Gravitational and mechanical forces drive mitochondrial translation through the cell adhesion–FAK axis

Taisei Wakigawa[1,2,9], Yusuke Kimura[1,2,9], Mari Mito[2], Toshiya Tsubaki[3], Hironori Saito[1,2], Abdul Haseeb Khan[4], Tohru Yamamori[5], Tomokazu Yamazaki[6], Akira Higashibata[6], Tatsuhisa Tsuboi[4,7], Taku Saito[3], Atsushi Higashitani[8], Yuichi Shichino[2], and Shintaro Iwasaki[1,2,10†]

[1]Department of Computational Biology and Medical Sciences, Graduate School of Frontier Sciences, The University of Tokyo, Kashiwa, Chiba 277-8561, Japan

[2]RNA Systems Biochemistry Laboratory, RIKEN Cluster for Pioneering Research, Wako, Saitama 351-0198, Japan

[3]Sensory & Motor System Medicine, Graduate School of Medicine, The University of Tokyo, Bunkyo-ku, Tokyo 113-8655, Japan

[4]Institute of Biopharmaceutical and Health Engineering, Tsinghua Shenzhen International Graduate School, Shenzhen 518055, China

[5]Japan Space Forum, Chiyoda-ku, Tokyo 101-0062, Japan

[6]JEM Utilization Center, Human Spaceflight Technology Directorate, Japan Aerospace Exploration Agency, Tsukuba, Ibaraki 305-8505, Japan

[7]Tsinghua-SIGS & Jilin Fuyuan Guan Food Group Joint Research Center, Tsinghua Shenzhen International Graduate School, Shenzhen 518055, China

[8]Graduate School of Life Sciences, Tohoku University, Sendai, Miyagi 980-8577, Japan

[9]These authors contributed equally.

[10]Lead contact

[†]Correspondence: shintaro.iwasaki@riken.jp (S.I.)

Abstract

Life on Earth has evolved in a form suitable for the gravitational force of 1 × *g*. Although the pivotal role of gravity in gene expression has been revealed by multiomics approaches in space-flown samples and astronauts, the molecular details of how mammalian cells harness gravity have remained unclear. Here, we show that mitochondria utilize gravity to activate protein synthesis within the organelle. Genome-wide ribosome profiling unveiled reduced mitochondrial translation in mammalian cells and *Caenorhabditis elegans* under microgravity in the International Space Station and under simulated microgravity in the 3D-clinostat on the ground. In addition, we found that cell adhesion through laminin–integrin interaction, which is attenuated by microgravity, and the downstream FAK, RAC1, PAK1, BAD, and Bcl-2 family proteins relay the signals for mitochondrial protein synthesis. Consistent with the role of integrin as a mechanosensor, we observed the decrease in mitochondrial translation by minimization of mechanical stress in mouse skeletal muscle. Our work provides mechanistic insights into how cells convert gravitational and mechanical forces into translation in an energy-producing organelle.

Introduction

Since the 1950s, when the first dog was flown into space, biological and medical research has revealed the unique responses of life in the space environment (*1*). In addition to radiation, microgravity is one of the main hazards to cells in space, potentially causing oxidative stress (*2*, *3*), mitochondrial dysfunction (*3–5*), and epigenetic changes (*5*, *6*). However, due to the constraints of spaceflight experiments, the global view of the cell response to microgravity is still far from complete.

To fill this gap, diverse omics approaches have been conducted with a cohort of flight samples, including ones from astronauts (*7*, *8*). These studies explored the epigenome, transcriptome, proteome, and metabolome (*3*, *9–18*) and indicated microgravity-mediated gene expression profile changes associated with the hazardous phenotypes mentioned above. However, these conventional spaceflight studies have lacked investigation of translational regulation, an acute and inducible means to reprogram protein expression (*19–22*). Given that translational control typically is followed by transcriptome changes, dynamic shifts in the protein synthesis rate under microgravity could be envisioned, but the "translatome" has not been assessed in previous spaceflight studies.

Here, we comprehensively surveyed the translational response to microgravity in human tissue cultures and *Caenorhabditis elegans* in space and found that mitochondrial translation is dramatically reduced by microgravity. In elucidating the mechanism of the response, we found that cell adhesion by laminin–integrin and the downstream signaling transmission through FAK, RAC1, PAK1, BAD, and Bcl-2 family proteins relays gravitational force to mitochondrial translation. Considering that laminin–integrin functions physiologically as a mechanosensor, the microgravity response may be the

manifestation of an impairment of mechanical stress. Congruent with this scenario, we recapitulated the attenuation of mitochondrial translation in unloaded and immobilized mouse hindlimbs. This study disclosed the previously uncharacterized unique connection between the extracellular environment and translation.

Results

Mitochondrial translation repression under microgravity in space

To investigate the translational landscape under microgravity, we conducted genome-wide ribosome profiling on HEK293 cells cultured in the International Space Station (ISS) (Figure 1A). For this purpose, cells were first cultured under 1 × *g,* artificially generated by centrifugation in the ISS, and then under microgravity for 24 and 48 h (Figure 1A). In contrast, control cells were maintained at 1 × *g* until harvest. Cells were treated with translation inhibitors (cycloheximide and chloramphenicol), frozen, and returned to the laboratory on Earth for library preparation.

Due to the restrictions of space flight, the amount of material that we could use was limited for standard ribosome profiling experiments. To overcome this issue, we harnessed Thor-Ribo-Seq, a ribosome profiling derivative tailored for low input based on RNA-dependent RNA amplification by *in vitro* transcription (*23*). The application allowed us to obtain high-quality data with samples returned from the ISS, which presented hallmarks of ribosome footprints: a sharp peak of read length at 28-29 nt (Figure S1A), 3-nt periodicity (Figure S1B), and high reproducibility (Figure S1C left).

As a result, our analysis revealed the impacts of microgravity on translation, especially the reduction in a subset of mRNAs (Figures 1B left, S1D left, and S1E). Among those, we found that protein synthesis from mitochondrial mRNAs, which are encoded in the organelle genome, was remarkably sensitive to microgravity (Figure 1B left). Since our method captured the footprints from both cytosolic ribosomes (cytoribosomes) and mitochondrial ribosomes (mitoribosomes) (*24*, *25*), we could interrogate both translation systems simultaneously. The reduction in mitoribosome footprints could not be explained by a reduction in the corresponding mRNAs, measured

by RNA sequencing (RNA-Seq) from the same materials (Figures 1B middle, S1C right, S1D middle, and S1E). Thus, the translation efficiency, calculated by over- or underrepresentation of ribosome footprints over RNA-Seq fragments, still showed a decrease in mitochondrial mRNAs (Figure 1B right). In contrast, the translation of mitochondria-localized proteins encoded in the nuclear genome was insensitive to microgravity (Figure S1F and S1G).

Mitochondrial translation regulation may be an early response to microgravity. Along the time course of the microgravity culture, we observed that the mitochondrial translation alteration was more dramatic at 24 h of incubation under microgravity than at 48 h (Figure 1C) (see Discussion for details).

To further extend our exploration from cell cultures to the whole-body level, we used nematode samples flown in the ISS (*16*). The L1 larvae were cultured under microgravity for 4 d, while the control worms were incubated in a 1 × *g* centrifuge (Figure 1D). As in human cells, ribosome profiling and RNA-Seq in nematodes (Figure S1I-K) unveiled the translational alteration in a subset of mRNAs (Figure S1L-M). Remarkably, we observed a reduction in mitochondrial translation efficiency (Figure 1E), as discovered in the cell-based experiments.

Through these spaceflight experiments, we concluded that mitochondrial translation attenuation is a pervasive response to microgravity in higher eukaryotes.

The mitochondrial translation response is recapitulated by simulated microgravity on the ground

To survey microgravity-mediated mitochondrial translation repression in the laboratory on the ground, we harnessed a clinostat that rotates the cell culture flask in three dimensions to reduce gravitational forces on the cells and simulate microgravity conditions (Figure 2A). Ribosome profiling and RNA-Seq of HEK293 cells revealed that the simulated microgravity phenocopied the attenuated mitochondrial translation observed in the ISS (Figures 2B, 2C, and S2A); we detected the reduction in mitoribosome footprints even at 1 h of simulated microgravity treatment. Again, we did not find a significant impact on nuclear genome-encoded mitochondrial localized proteins (Figure S2B and S2C). Gravity-mediated mitochondrial translation regulation was further ensured by mitochondria-specific fluorescent noncanonical amino acid tagging on gel (on-gel mito-FUNCAT) (*26–30*) (Figure 2D). Since the same molecular phenotype was observed in human cells (HEK293) and mouse cells (C2C12 and 3T3) (Figures 2D and S2D), the mitochondrial translation response to microgravity is likely driven by conserved mechanisms.

Our on-gel mito-FUNCAT experiments showed that mitochondrial translation is a function of gravity. When the cell culture was returned to standard 1 × *g*, the mitochondrial translation reduced by microgravity was restored to the baseline level, suggesting the elasticity of the mechanism (Figure 2E). Moreover, 10 × *g* hypergravity, induced by centrifugation, resulted in the activation of mitochondrial translation (Figure 2F), whereas 1 × *g* centrifugation did not (Figure S2E).

Given that microgravity-mediated oxidative stress has been reported (*2–4*), we investigated the correspondence between mitochondrial oxidative stress and *in organello* protein synthesis under microgravity. We could not observe a significant alteration in the copy number of mitochondrial DNA, which is susceptible to oxidative damage (Figure

S2F and S2G). Moreover, our microscopic analysis did not detect mitochondrial fragmentation, which could be induced by mitochondrial oxidative stress (*31*, *32*) (Figure S2H and S2I). Furthermore, we could not find the signature of the mitochondrial unfolded protein response (mtUPR) (*33*) since the transcriptomic alteration of targets (*34*) was limited in both space and clinostat samples (Figures S1H and S2J). Thus, our data indicated that mitochondrial translation repression is not caused by oxidative stress or morphological defects in the organelle.

The cell adhesion pathway relays gravitic force to mitochondrial translation

How do cells recognize gravity and transmit the information to organelle translation? Recent studies have highlighted the attenuation of cell adhesion and subsequent signal transduction through the focal adhesion kinase (FAK) pathway by microgravity (*35*–*37*). Consistent with these reports, we observed that the phosphorylation of FAK, which is driven by cell adhesion, was reduced by simulated microgravity (Figure S3A). Thus, we reasoned that modulated cell adhesion may reduce mitochondrial translation in microgravity.

We first investigated the relationship between cell adhesion and organellar translation under regular gravity. Considering the translation flux of the α and β subunits of integrin, a receptor of the extracellular matrix (ECM), the laminin receptor $\alpha_6\beta_1$ was an abundant class in HEK293 cells (Figure S3B). Accordingly, the pretreatment of cell culture dishes with laminin-511 (or $\alpha_5\beta_1\gamma_1$), which shows a high affinity for $\alpha_6\beta_1$ integrin (*38*, *39*), enhanced the cell adhesion activity in a dose-dependent manner (Figure 3A and 3B top) and thus elevated FAK phosphorylation level (Figure S3C). Through on-gel mito-

FUNCAT, we found that mitochondrial protein synthesis was concomitantly activated by increasing the laminin concentration (Figure 3A and 3B bottom left) and correlated with cell adhesion activity (Figure 3B bottom right). Similar mitochondrial translation activation by laminin was observed in other cell types (human HAP1 and mouse C2C12 and 3T3) as well (Figures 3C, 4H, and S3D). Conversely, mitochondrial translation was inhibited by RGDS peptide, an integrin inhibitor (Figure 3D), associated with FAK dephosphorylation (Figure S3E). In contrast to *in organello* translation, total protein synthesis, which predominantly originates from cytosolic translation, was altered by neither laminin nor RGDS peptide treatments (Figure 3B-D). These results showed that cell adhesion specifically enhances mitochondrial translation.

To test whether microgravity-mediated mitochondrial translation repression is caused by reduced cell adhesion, we pretreated a cell culture flask with laminin, cultivated the cells with simulated microgravity, and then conducted ribosome profiling and RNA-Seq. Strikingly, the laminin counteracted the effect of microgravity on mitochondrial protein synthesis (Figure 3E). We concluded that cell adhesion is a mediator of gravitational forces to organellar translation.

The loss of *in organello* translation homeostasis results in physiological dysfunction of the organelle. Attenuated cell adhesion by RGDS peptides hampered the oxygen consumption rate of the mitochondria (Figure 3F), as did the mitochondrial translation inhibitor chloramphenicol. Moreover, metabolites associated with the tricarboxylic acid (TCA) cycle were reduced by simulated microgravity (Figure 3G). These data suggested that mitochondrial translation facilitated by cell adhesion and gravity is required to maintain the metabolic integrity of the organelle.

FAK–RAC1–PAK1–BAD–Bcl-2 family protein axis conveys the cell adhesion signal to mitochondrial protein synthesis

Given the phosphorylation and activation of FAK upon laminin–integrin interaction (*40*, *41*) (Figure S3C), we investigated the significance of this factor for mitochondrial translation. Indeed, FAK knockdown resulted in the loss of laminin-mediated activation of *in organello* translation (Figures 4A and S4A).

We asked how the downstream signaling pathway(s) of FAK connects to mitochondria. Since FAK influences widespread enzymes such as small GTPases (RAC1, CDC42, RHOA, KRAS), phosphatidylinositol 3-kinase (PI3K), and Jun N-terminal kinase (JNK) (*40*, *41*) (Figure S4B), those activities were pharmacologically inhibited (Figure S4C), and the potential of laminin-mediated mitochondrial translation activation was evaluated by on-gel mito-FUNCAT. Screening showed that RAC1 inhibition specifically hampered laminin-mediated mitochondrial translation activation (Figures 4B and S4D). As expected, laminin treatment accumulated the active GTP-bound form of RAC1 (Figure 4C), which is evoked by phosphorylated FAK (*40*, *41*).

Further compound treatment narrowed the downstream pathway of RAC1 (*42*) to PAK1 but not ARP2/3 (Figures 4D, S4E, and S4F). We observed elevated phosphorylation of PAK1, which is mediated by GTP-activated RAC1 (*42*), in laminin-treated cells (Figure 4E).

Given that PAK1 couples with the pro-survival cascade driven by Bcl-2 family proteins on the mitochondrial outer membrane (*43–45*), we reasoned that the Bcl-2 family pathway may participate in cell adhesion-mediated mitochondrial translation activation. We treated cells with pan-Bcl-2 family inhibitors (such as obatoclax and TW-37)

inhibitors and found that the effect of laminin on mitochondrial protein synthesis was counteracted (Figures 4F, S4G, and S4H).

To regulate Bcl-2 family proteins, PAK1 phosphorylates BAD (*46*), one of the pro-apoptotic Bcl-2 homology 3 (BH3)-only proteins, which binds to Bcl-2 family proteins and inhibits the pro-survival effect (*47–49*). BAD phosphorylation reduces its affinity to Bcl-2 family proteins, dissociating BAD from Bcl2 proteins and thus from the mitochondrial outer membrane (*47–49*). Indeed, laminin treatment decreased the mitochondria-associated fraction of BAD (Figure 4G).

Given that, we examined the role of BAD in mitochondrial translation. During our analysis of the knockout of *BAD* in HAP1 cells (Figure S4I), we noticed that the reduction of mitochondrial mass in this cell line (data not shown and Figure S4J right). To normalize mitochondrial volume and simultaneously detect the protein synthesis rate in the organelle, we harnessed mito-FUNCAT fluorescence-activated cell sorting (FACS) (*29*). The mito-FUNCAT FACS revealed that the deletion of *BAD* resulted in a high level of net mitochondrial translation due to the loss of the suppression mechanism for mitochondrial translation (Figures 4H and S4J). Because of the constitutive activation of mitochondrial translation even in the absence of laminin treatment, *BAD* deficiency led to an attenuated response to laminin for the activation of mitochondrial translation monitored by on-gel mito-FUNCAT (Figure 4I).

The pathway that we discovered here should be independent of the known regulatory mechanisms for mitochondrial translation. Membrane potential is a prerequisite for mitochondrial protein synthesis (*50–52*) (Figure S4K). However, alterations in membrane potential could not explain the dynamics of mitochondrial translation upon cell adhesion modulation (Figure S4L-O). In yeast, rapid communication

between cytosolic and mitochondrial translation systems has been reported (*53*); cytosolic translation synchronizes its output with mitochondrial protein synthesis. However, our ribosome profiling did not show a large alteration in OXPHOS complex subunits or mitochondria-localized proteins encoded in the nuclear genome (Figures S1F and S2B). Moreover, a recent report suggested that the synchronization mechanism is not conserved in humans (*54*).

Mechanical stress enhances mitochondrial protein synthesis in vivo

The correspondence between mitochondrial translation and laminin–integrin-mediated cell adhesion led us to study the physiological significance of this cascade. Considering that integrin plays a critical role as a mechanosensor (*55–58*), we hypothesized that mechanical stress promotes mitochondrial translation. Given that mechanical stress and gravity maintain skeletal muscle homeostasis and FAK phosphorylation (*35–37*, *59*, *60*), we focused on translation in the tissue of mice. In a minimized mechanical stress (MMS) model, the mice underwent hindlimb unloading and immobilization, and the soleus was subjected to ribosome profiling and RNA-Seq (Figure 5A). Along the duration of the MMS, we found reduced mitochondrial translation at 14 d after the start of the minimized mechanical stress (Figure 5B and 5C), the time when we detected the reduced muscle weight (Figure S5A). Our results indicated the importance of mechanical stress for mitochondrial protein synthesis.

Discussion

Starting from the translatome analysis of space-flown samples, we elucidated a previously unexplored cell signaling pathway that connects cell adhesion sensing and *in organello* translation (Figure 5D). Although the mediation of translational reprogramming by integrin and mechanical force has been suggested for decades (*61–63*), the landscape has remained largely unclear. Our study unveiled mitochondrial translation as a subject of regulation. In muscle, which is constantly subjected to mechanical stresses through loading, postural maintenance, and exercise, this system enables rational regulation of energy production in mitochondria: increased mechanical stresses lead to increased mitochondrial protein synthesis and thus modulate the organelle functions.

Although the short-term microgravity in our study did not provide strong evidence, long-term culture under microgravity may ultimately lead to mitochondrial damage. Indeed, the recent multiomics approach conducted by NASA's GeneLab covering astronaut cohort and space-flown samples (*3*) illustrated mitochondrial damage as a hallmark of spaceflight. The attenuation of mitochondrial translation may prime the damage processes in space.

Intriguingly, at 48 h of microgravity exposure, we observed the recovery of translation efficiency for mitochondrial mRNAs (Figure 1C right), suggesting adaptation to the microgravity environment. This may be due to the constant reduction in mRNAs (Figure 1C middle), allowing the longstanding suppression of mitochondrial protein production. On the other hand, this adaptation did not occur in the simulated microgravity at least for 72 h (Figure S5B). This may be due to the lesser magnitude of the effect caused by simulated microgravity than by bona fide microgravity in the ISS (compare the y-axis

scales in Figures 1C and 2C), probably owing to the "time-averaged" microgravity in the 3D clinostat.

By small-scale chemical screening, we outlined the signal cascade from cell adhesion to the mitochondrial outer membrane (Figure 5D). Earlier studies indicated that PAK1 phosphorylates BAD in two pathways: directly or indirectly through Raf1 (*46*). Since we could not find a significant effect of the Raf1 inhibitor (Figure S5C-E), direct phosphorylation by PAK1 may be a major pathway under our conditions, although our data did not exclude a variable balance of the direct and indirect pathways across cells. Although the pan-Bcl2 family protein inhibitors obatoclax and TW-37 blocked laminin-activated mitochondrial translation (Figure 4F), the same phenotype was not observed for the compounds specific for each Bcl-2 family protein (Figure S5F-H), suggesting that Bcl-2 family proteins perform redundant functions in mitochondrial translation enhancement.

In contrast to the signal pathway from integrin to Bcl-2 family proteins at the mitochondrial outer membrane, it remains unclear how the signal is transduced into the mitochondrial matrix and how protein synthesis in the matrix is regulated. The pro-survival role of Bcl-2 family proteins relies on their binding to BAX to suppress BAX oligomerization, a driver of the apoptosis cascade. However, the function of the Bcl-2 family in mitochondrial translation activation may not be based on this conventional mechanism, since neither the BAX activator nor the inhibitor impacted mitochondrial translation (Figure S5I-K).

Our study sheds light on the unique translational response in bioenergetic powerhouses to external gravitational and mechanical forces.

Acknowledgments

We thank all the members of the Iwasaki laboratory for constructive discussion, technical help, and critical reading of the manuscript. We are also grateful to Yasuhiro Nakamura (Japan Aerospace Exploration Agency, JAXA), Toru Shimazu (Japan Space Forum), Hiromi Sano (Japan Manned Space Systems Corporation, JAMSS), and Ikuko Osada (JAMSS) for the administrative and technical help with the spaceflight experiments (termed "Ribosome Profiling"). The ground operation for the spaceflight experiments was supported by the JAXA Flight Control Team and Payload Flight Control Team. The experiments in the ISS were conducted by Soichi Noguchi. FACS analysis was supported by Kenji Ohtawa from the Support Unit for Bio-Material Analysis, RIKEN CBS Research Resources Division. Microscopic analysis was supported by RIKEN CBS-Olympus Collaboration Center. A part of the deep sequencing analysis was conducted by the Vincent J. Coates Genomics Sequencing Laboratory at UC Berkeley, supported by the NIH S10 OD018174 Instrumentation Grant. This work used the supercomputer HOKUSAI SailingShip in RIKEN. Mouse 3T3 cells were gifts from Shinichi Nakagawa. S.I. was supported by the Japan Society for the Promotion of Science (JSPS) (a Grant-in-Aid for Young Scientists [A], JP17H04998; a Challenging Research [Exploratory], JP19K22406), the Ministry of Education, Culture, Sports, Science and Technology (MEXT) (a Grant-in-Aid for Transformative Research Areas [B] "Parametric Translation", JP20H05784), the Japan Agency for Medical Research and Development (AMED) (AMED-CREST, 22gm1410001), Gushinkai Foundation, and RIKEN ("Biology of Intracellular Environments" and "Integrated life science research to challenge super aging society"). Y.K. was supported by JSPS (a Grant-in-Aid for JSPS Fellows, JP20J10665). T.W. was supported by The Graduate School of Frontier Sciences,

The University of Tokyo (the Challenging New Area Doctoral Research Grant, C2205). Y.S. was supported by JSPS (a Grant-in-Aid for Early-Career Scientists, JP21K15023), MEXT (a Grant-in-Aid for Transformative Research Areas [A] "Multifaceted Proteins", JP21H05734), and RIKEN (Special Postdoctoral Researchers and Incentive Research Projects). T. Tsuboi acknowledges support from the Jilin Fuyuan Guan Food Group Co., Ltd, the Science, Technology, Innovation Commission of Shenzhen Municipality (WDZC20220811144737001), and startup funds from Tsinghua SIGS. We also thank the fellowship foundations (the RIKEN Junior Research Associate Program for Y.K. and H.S.; the JSPS Research Fellow [DC2] for Y.K.; JST SPRING [JPMJSP2108] for T.W. and T. Tsubaki; and the ANRI fellowship for T.W.).

Author contributions

Conceptualization, T.W., Y.K., T. Yamamori, T. Yamazaki, A. Higashibata, and S.I.;

Methodology, T.W., Y.K., M.M., T. Tsubaki, H.S., A.H.K., T. Yamamori, T. Yamazaki, A. Higashibata, T. Tsuboi, T.S., A. Higashitani, Y.S., and S.I.;

Formal analysis, T.W., Y.K., M.M., T. Tsubaki, H.S., A.H.K., and T. Tsuboi;

Investigation, T.W., Y.K., M.M., T. Tsubaki, and H.S.;

Resources, A. Higashibata and A. Higashitani;

Writing – Original Draft, T.W., Y.K., and S.I.;

Writing – Review & Editing, T.W., Y.K., M.M., T. Tsubaki, H.S., A.H.K., T. Yamamori, T. Yamazaki, A. Higashibata, T. Tsuboi, T.S., A. Higashitani, Y.S., and S.I.;

Visualization, T.W. and S.I.;

Supervision, T. Yamamori, T. Yamazaki, A. Higashibata, T. Tsuboi, T.S., A. Higashitani, Y.S., and S.I.;

Funding Acquisition, T.W., Y.K., T. Tsuboi, Y.S., and S.I.

Experimental procedures

Cell culture

HEK293 cells (ATCC, CRL-1573), C2C12 cells (ATCC, CRL-1772), 3T3 cells (kind gifts from Shinichi Nakagawa's laboratory), naïve HAP1 cells (Horizon Discovery, C631), and *BAD* KO HAP1 cells (Horizon Discovery, 29-bp deletion, HZGHC005959c002) were cultured in DMEM (high glucose, GlutaMAX Supplement, Thermo Fisher Scientific, 10566016) with 10% FBS (Sigma–Aldrich) (for HEK293, C2C12, and 3T3) or IMDM (GlutaMAX Supplement, Thermo Fisher Scientific, 31980030) with 10% FBS (Sigma–Aldrich) (for HAP1) at 37°C with 5% CO_2, according to the manufacturer's instructions. The *Mycoplasma*-free culture was confirmed by an e-Myco VALiD Mycoplasma PCR Detection Kit (iNtRON Biotechnology). A disposable cultivation chamber (DCC) (JAXA and Chiyoda Corporation) (*64*) was used to culture the cells on the 3D clinostat (5.5 rpm at X axis and 6.5 rpm at Y axis, AES) and the centrifuge (AES). The DCC was completely filled with medium to prevent shear stress caused by air bubbles.

Compounds

Cells were treated with the following compounds at the indicated concentrations: cycloheximide (Sigma–Aldrich, C4859, 100 μg/ml), chloramphenicol (FUJIFILM Wako Pure Chemical Corporation, 030-19452, 100 μg/ml), anisomycin (Alomone Labs, A-520, 100 μg/ml), RGDS peptide (Tocris, 3498, 10 μg/ml), NSC23766 (Tocris, 2161, 200 μM), ZCL278 (Tocris, 4794, 100 μM), Rhosin (Tocris, 5003, 50 μM), BAY-293 (Tocris, 6857, 1 μM), LY294002 (Sigma–Aldrich, L9908, 10 μM), SP600125 (Sigma–Aldrich, S5567, 20 μM), IPA-3 (Tocris, 3622, 5 μM), CK666 (Tocris, 3950, 25 μM), obatoclax

(Selleckchem, S1057, 2 μM), TW-37 (Selleckchem, S1121, 10 μM), valinomycin (Tocris, 3373, 2 μM), sorafenib (Selleckchem, S1040, 1 μM), GW5074 (Tocris, 1381, 5 μM), ZM336372 (Tocris, 1321, 10 μM), venetoclax (Selleckchem, S8048, 10 μM), A-1331852 (Selleckchem, S7801, 10 μM), S63845 (Selleckchem, S8383, 5 μM), BAI1 (Tocris, 2160, 1 μM), BTSA1 (Selleckchem, S8650, 20 μM), and BAM7 (Tocris, 4810, 20 μM). Chloramphenicol was dissolved in 70% ethanol, and the others were dissolved in dimethyl sulfoxide (DMSO).

Spaceflight experiments

DCCs were pretreated with laminin overnight as described below. Then, 5×10^5 HEK293 cells were seeded in each DCC and incubated overnight. The medium was exchanged to CELLBANKER 1 plus (TaKaRa) and stored at −80°C. The frozen cells were launched to the ISS by Cygnus NG-14 in October 2020. In the Japanese Experiment Module KIBO in the ISS, the samples were thawed, exchanged to DMEM, high glucose, GlutaMAX Supplement (Thermo Fisher Scientific) with 10% FBS using Pre-Fixation Kit-III (PFK-III, JAXA) (*64*), and cultured under centrifugation at 1 × *g* in the Cell Biology Experiment Facility (CBEF) (*65*) at 37°C with 5% CO_2 and 80±5% RH for 24 h. Subsequently, the cells were cultured under microgravity for 24 and 48 h, while the control cells were maintained at 1 × *g*. For chemical fixation, cell culture media were replaced with CELLBANKER 1 plus containing 100 μg/ml cycloheximide and 100 μg/ml chloramphenicol by PFK-III. Then, the samples were stored in a Minus Eighty degree Celsius Laboratory Freezer for ISS (MELFI) at −95°C. Samples were returned to the ground by SpaceX CRS-22 (SpX-22) in July 2021, maintaining their frozen status, and were stored at −80°C in the laboratory for ribosome profiling and RNA-seq..

Space-flown *C. elegans* samples prepared for earlier experiments (*16*) were used in this study.

Animals

All animal experiments were authorized and approved by the Animal Care and Use Committee of The University of Tokyo. Adult male (7 weeks old) C57BL/6J mice were purchased from Sankyo Lab Service Corporation, housed in the facility under the supervision of the IACUC at 18 to 22°C with a 12-h:12-h light-dark cycle, and allowed free access to food and water.

Minimized mechanical stress (MMS)

The MMS model was developed by one of the co-authors and will be published elsewhere. First, we applied adhesive tape to the tails of 8 week-old mice. Their knee joints were then kept immobilized using plastic cylinders. Their feet were also taped up to prevent the plastic cylinders from sliding off. Additional adhesive tape was applied between the rear limbs so that the mice could not bite the adhesive tape around their tail. Following joint fixation, their tails were suspended by attaching a spring clip to the adhesive tape. The spring clip was connected to piano wire that was attached to the cage lid, so that the mice could move in their cages. Food was left on the floor and a water bottle was fixed to the wall with double-sided tape for easy access.

Mice were sacrificed at 1, 3, and 14 d after MMS started. For the control, age-matched mice were harvested (8 weeks old and 10 weeks old). The soleus muscles were dissected and the wet weights were measured. The muscles were immediately flash-frozen by liquid nitrogen and stored at −80°C.

Ribosome profiling and RNA-Seq

Lysate preparation

Spaceflight samples, HEK293:

Cells in a DCC were thawed, washed with ice-cold PBS, lysed with 500 µl of lysis buffer (20 mM Tris-HCl pH 7.5, 150 mM NaCl, 5 mM $MgCl_2$, 1 mM dithiothreitol [DTT], 1% Triton X-100, 100 µg/ml cycloheximide, and 100 µg/ml chloramphenicol), and triturated ten times in a syringe with a 30-gauge needle (NIPRO CORPORATION). The lysate was incubated with 25 U/ml TURBO DNase (Thermo Fisher Scientific) and clarified by centrifugation at 20,000 × *g* for 10 min at 4°C.

Spaceflight samples, C. elegans:

Frozen nematode culture (1.5-4.5 ml) was thawed in 10 ml of wash buffer (20 mM Tris-HCl pH 7.5, 150 mM NaCl, 5 mM $MgCl_2$, 100 µg/ml cycloheximide, and 100 µg/ml chloramphenicol). The adult worms were filtrated through a 30-µm ÜberStrainer (pluriSelect Life Science) and washed three times with wash buffer. Then, the nematodes were pelleted by centrifugation at 1,600 × g for 1 min at 4°C, resuspended in 600 µl of lysis buffer, and dripped into liquid nitrogen. After pulverization using the Multi-beads Shocker at 2800 rpm for 10 sec (Yasui Kikai), the lysate was thawed at 4°C, incubated with 25 U/ml Turbo DNase (Thermo Fisher Scientific), and clarified by centrifugation at 20,000 × g for 10 min at 4°C.

Simulated microgravity samples:

Cells in DCC were washed with PBS and lysed with 500 µl of lysis buffer. After 25 U/ml TURBO DNase treatment (Thermo Fisher Scientific), the lysate was clarified by centrifugation at 20,000 × g for 10 min at 4°C.

Mouse soleus muscles:

Frozen soleus muscles were pulverized with 600 µl of frozen lysis buffer containing cOmplete, EDTA-free Protease Inhibitor Cocktail (Roche) and 1000 U/ml RNase inhibitor, Murine (New England Biolabs [NEB]), using the Multi-beads Shocker at 3000 rpm for 30 sec for 2 cycles (Yasui Kikai). After thawing at 4°C, the lysate was incubated with 25 U/ml Turbo DNase (Thermo Fisher Scientific) and clarified by centrifugation at 20,000 × g for 10 min at 4°C.

Library preparation for ribosome profiling

For simulated microgravity samples, ribosome profiling library preparation was performed as previously described (*66*). The other libraries were generated by the Thor-Ribo-Seq protocol as described earlier (*23*).

The lysate was treated with 20 U of RNase I (LGC Biosearch Technologies) at 25°C for 45 min. A sucrose cushion was used to collect ribosomes. The RNA was run on a 15% UREA PAGE gel. RNA fragments ranging from 17 to 34 nucleotides (nt) were excised from the gel, dephosphorylated, and ligated with linkers. rRNAs were depleted with the Ribo-Zero Gold rRNA Removal Kit (Human/Mouse/Rat) (Illumina) for human and mouse samples and with *Caenorhabditis elegans* Ribo-Seq riboPOOLs (siTOOLs Biotech) for nematode samples. For simulated microgravity samples, cDNA was synthesized by reverse transcription, circular-ligated, and PCR-amplified. For the other

samples, after hybridization of an oligonucleotide to the T7 promoter region of the linker, complementary RNAs were transcribed by a T7-Scribe Standard RNA IVT kit (CELLSCRIPT) and then ligated to the second linker. cDNA was reverse-transcribed and PCR-amplified. The DNA libraries were sequenced on a HiSeq 4000 with 50-bp single-read mode (s-µg experiments) or a HiSeq X Ten in 150-bp pair-end mode (the other experiments).

Library preparation for RNA-Seq

For RNA-seq, total RNA was extracted from the same lysate used for ribosome profiling with TRIzol LS (Thermo Fisher Scientific) and a Direct-zol RNA Microprep Kit (Zymo Research). rRNA depletion was conducted with the Ribo-Zero Gold rRNA Removal Kit (Human/Mouse/Rat) (Illumina) for human and mouse samples and with *Caenorhabditis elegans* Ribo-Seq riboPOOLs (siTOOLs Biotech) for nematode samples.

For HEK293 cells for spaceflight experiments and mouse soleus muscles, the libraries were prepared by SMARTer Stranded Total RNA-Seq Kit v3 - Pico Input (TaKaRa). The other RNA-Seq libraries were generated by a TruSeq Stranded mRNA Library Prep kit (Illumina). The DNA libraries were sequenced on a HiSeq 4000 with 50-bp single-read mode (s-µg experiments) or a HiSeq X Ten in 150-bp pair-end mode (the other experiments).

Data analysis

Data were processed as described previously (*25*, *67*) with modifications. For ribosome profiling with pair-end sequencing, base correction was performed by Fastp (version 0.21.0) (*68*) and read 1 was used for downstream analysis. After read quality filtering and

adapter trimming by Fastp, all reads aligned to non-coding RNAs (rRNAs, tRNAs, mt-rRNAs, mt-tRNAs, snRNAs, snoRNAs, and miRNAs) were removed using STAR (version 2.7.0a) (*69*). Then, the reads were mapped to the corresponding nuclear genomes (human, hg38; mouse, mm10; *C. elegans*, WBcel235) and custom-made mitochondrial transcript sequences by STAR. UMI suppression in Thor-Ribo-Seq was performed using UMItools (version 1.1.2) (*70*). For ribosome profiling, ribosomal A-site position offsets from the 5′ end of reads were empirically estimated along the read length as summarized in Table S1. For RNA-Seq, the offset was set to 15.

To count reads from CDS, reads assigned to the first and last 5 amino acids were excluded. The relative enrichments of reads across CDSs in ribosome profiling and RNA-Seq were calculated by the DESeq2 package (*71*). Additionally, translation efficiency was calculated by a generalized linear model with the same package. Gene Ontology analysis was performed with DAVID (https://david.ncifcrf.gov/home.jsp) (*72*, *73*). Mitocarta3 genes were defined in (https://www.broadinstitute.org/files/shared/metabolism/mitocarta/human.mitocarta3.0.html) (*74*). mtUPR target genes were defined in an earlier work (*34*).

Laminin coating

DCCs, 6-well plates, 12-well plates, and 96-well plates were precoated with 0.25 μg/cm^2 (or dilutions as indicated in the figures) laminin (Easy iMatrix-511 silk, MATRIXOME) overnight at 4°C before cell seeding.

Cell adhesion assay

Each well of the 96-well plate was precoated with laminin as described above. One hundred microliters of HEK293 cell suspension (5×10^5 cells/ml) was seeded and incubated for 1 h in a CO_2 incubator. After washing out the unattached cells with PBS, the adhered cells were fixed with 4% (w/v) paraformaldehyde in PBS for 20 min, permeabilized with 0.1% Triton X-100 in PBS, and stained with 0.2 μM CellTag 700 (LI-COR Biosciences) for 1 h. Images were acquired by Odyssey CLx (LI-COR Biosciences) with an IR 700-nm channel.

On-gel mito-FUNCAT

On-gel mito-FUNCAT was conducted as described previously (*29*). Cells were seeded on dishes with or without laminin coating and incubated for 12 h with the indicated compounds before cell harvest. Nascent peptides were labeled with 50 μM HPG (Jena Bioscience) in methionine-free medium (DMEM, high glucose, no glutamine, no methionine, no cystine [Thermo Fisher Scientific], supplemented with 48 μg/ml L-cysteine and 4.08 mM L-alanyl-L-glutamine) with 100 mg/ml anisomycin for 3 or 4 h. Cells were washed with ice-cold PBS and lysed with FUNCAT lysis buffer (20 mM Tris-HCl pH 7.5, 150 mM NaCl, 5 mM $MgCl_2$, and 1% Triton X-100). After clarification by centrifugation at 20,000 × g for 10 min at 4°C, the supernatants were incubated with 5 μM IRdye800CW Azide (LI-COR Biosciences) with a Click-it Cell Reaction Buffer Kit (Thermo Fisher Scientific) according to the manufacturer's instructions and run on SDS–PAGE gels. Images were acquired by an Odyssey CLx (LI-COR Biosciences) with an IR 800-nm channel. For signal normalization, gels were stained with EzStain AQua (ATTO) or GelCode Blue Safe Protein Stain (Thermo Fisher Scientific) to detect total proteins,

and images were acquired by Odyssey CLx with an IR 700-nm channel. The signals on gels were quantified with Image Studio (LI-COR Biosciences, version 5.2).

For the measurement of total protein synthesis, anisomycin was omitted from the experiments.

For knockdown experiments, cells were transfected with 5 μM siRNA targeting FAK (Horizon Discovery, L-003164-00-0005) or control siRNA (Horizon Discovery, D-001206-13-20) using TransIT-X2 Reagent (Mirus Bio, MIR6003) in 10-cm dishes and incubated for 24 h. Then, cells were reseeded on 12-well dishes with or without laminin coating as described above, cultured for an additional 24 h, and used for on-gel mito-FUNCAT experiments.

Mito-FUNCAT FACS

Mito-FUNCAT FACS was performed as described previously (*29*). HAP1 cells were cultured in methionine-free medium with 100 μM HPG and 100 mg/ml anisomycin for 3 h before cell harvest. After washing with PBS, cells were dissociated from the dish with 0.05% trypsin. The collected cells were washed, prepermeabilized with 0.0005% digitonin in mitochondrial protective buffer (10 mM HEPES-KOH pH 7.5, 300 mM sucrose, 10 mM NaCl, and 5 mM $MgCl_2$) for 5 min at room temperature, fixed in 4% paraformaldehyde (PFA) for 15 min at 4°C, and permeabilized with 0.1% (v/v) Triton X-100 in PBS for 5 min at room temperature. Subsequently, nascent peptides within mitochondria were labeled with 1 μM azide-conjugated Cy3 (Jena Bioscience) with a Click-it Cell Reaction Buffer Kit (Thermo Fisher Scientific). Mitochondria were immunostained with Alexa Fluor 647 Anti-TOMM20 antibody (Abcam, ab209606, 1:100) in Intercept Blocking Buffer (LI-COR Biosciences) for 1 h at 4°C. Cells were

washed three times with PBS and then analyzed with flow cytometry (BD FACSAria II, BD Biosciences).

Mitochondrial DNA content measurement

Total DNA was extracted from 1 × 10^6 cells using NucleoSpin DNA RapidLyse (MACHEREY-NAGEL). qPCR was performed with primers targeting the ND2 locus in the mitochondrial genome (5′-TGTTGGTTATACCCTTCCCGTACTA-3′ and 5′-CCTGCAAAGATGGTAGAGTAGATGA-3′) and those targeting the Alu repeat sequence in the nuclear genome (5′-CTTGCAGTGAGCCGAGATT-3′ and 5′-GAGACGGAGTCTCGCTCTGTC-3′) (*75*) with TB Green Premix Ex Taq II (TaKaRa) on Thermal Cycler Dice Real Time System II (TaKaRa). The relative mitochondrial DNA content normalized by nuclear-genome content was determined using the ΔΔCt method.

Microscopic analysis

Cells were cultured in a glass-bottom DCC (AES), washed with PBS, fixed with 4% (w/v) paraformaldehyde in PBS for 15 min at room temperature, and subsequently incubated with methanol for 10 min at −20°C. After washing twice with PBS, the cells were incubated with Intercept Blocking Buffer (LI-COR Biosciences) containing 0.2% Triton X-100 for 60 min at room temperature. Then, mitochondria were immunostained in Intercept Blocking Buffer with 0.2% Triton X-100 and Alexa Fluor 647 Anti-TOMM20 antibody (Abcam, ab209606, 1:100) for 1 h at room temperature. The cells were washed with TBS with 0.2% Triton X-100 three times and then incubated with VECTASHIELD Mounting Medium (VECTOR LABORATORIES, INC., H-1500) overnight at 4°C, protected from light. Images were obtained using an FV3000 confocal microscope

(Olympus) with a 60× objective lens (Olympus Japan, UPLXAPO60XO) and processes as described below.

Morphological quantification of mitochondria

Image analysis was performed using MitoGraph (version 3.0), a fully automated C++ program for 3D mitochondrial structure analysis (https://github.com/vianamp/MitoGraph) (*76*, *77*). We first isolated 3D images of individual cells from the raw images using the FIJI (https://fiji.sc) macro to extract cellular trends and then applied them as inputs to the MitoGraph software. For the MitoGraph parameter, we used 0.414 for the flag -xy and 0.3 for the flag -z.

Mitochondrial membrane potential assessment

Mitochondrial membrane potential was measured by flow cytometry as described previously (*78*). Cells were incubated with 200 nM Mitotracker Red CMXRos (Thermo Fisher Scientific) and 150 nM Mitotracker Green FM (Thermo Fisher Scientific) at 37°C for 25 min and then washed with PBS with 5% FBS. After dissociating cells from the dish with 0.05% trypsin and subsequent neutralization, cells were collected by centrifugation at 300 × g for 3 min, resuspended in PBS with 5% FBS, and then subjected to flow cytometry (BD FACSAria II, BD Biosciences).

Western blotting

Anti-β-actin (MEDICAL & BIOLOGICAL LABORATORIES [MBL], M177-3, 1:1000), anti-GAPDH (Cell Signaling Technology [CST], 2118, 1:1000), anti-FAK (CST, 3285, 1:1000; Thermo Fisher Scientific, AHO0502, 1:1000), anti-p-FAK^{Y397} (CST, 3283,

1:200), anti-TOMM20 (CST, 42406, 1:1000), anti-RAC1 (CST, 8631, 1:200), anti-PAK1 (CST, 2602, 1:1000), anti-p-PAK1^{S144}/p-PAK2^{S141} (CST, 2606, 1:200), and anti-BAD (CST, 9292, 1:200) were used as primary antibodies. IRDye800CW anti-rabbit IgG (LI-COR Biosciences, 926-32211, 1:10000) was used as a secondary antibody. Images were obtained with Odyssey CLx (LI-COR Biosciences) and quantified with Image Studio (LI-COR Biosciences, version 5.2).

Isolation of RAC1 in the GTP-bound form

RAC1 in the GTP-bound form was isolated with an Active Rac1 Detection Kit (CST, 8815) according to the manufacturer's instructions. Anti-RAC1 Western blotting was performed as described above.

Mitochondrial purification

Mitochondria were isolated with a Mitochondria Isolation Kit, Human (Miltenyi Biotec), according to the manufacturer's instructions with minor modifications. Cells were washed with ice-cold PBS and lysed with hypotonic buffer (10 mM HEPES-KOH pH 7.5, 10 mM KCl, 1.5 mM $MgCl_2$, and 1 mM DTT). The cell lysate was incubated with TOM22 beads for 60 min at 4°C. After washing, the mitochondrial fraction was eluted from the beads, pelleted by centrifugation at 7,000 × g for 10 min at 4°C, resuspended in modified lysis buffer (20 mM Tris-HCl, pH 7.5, 150 mM NaCl, 15 mM $MgCl_2$, 1 mM DTT, and 1% Triton X-100), and then centrifuged at 20,000 × g for 10 min at 4°C. The supernatant was used for Western blotting.

Cell viability assay

Cell viability was monitored as described previously (*79*). Cells were seeded on 96-well plates, treated with the indicated compounds for 12 h, and then incubated with RealTime-Glo MT Cell Viability Assay reagent (Promega) for 30 min. The luminescence was quantified by the GloMax Navigator System (Promega).

Oxygen consumption rate (OCR)

After culturing cells on Seahorse XFe96 cell culture microplates (Agilent), the medium was replaced with Seahorse XF DMEM (Agilent) containing 1 mM pyruvate, 2 mM glutamine, and 10 mM glucose and then incubated at 37°C for 1 h. OCR was monitored on a Seahorse XFe96 Analyzer (Agilent) throughout sequential injections of 0.5 μM oligomycin, 0.5 μM FCCP, and 0.5 μM rotenone/antimycin A into the cell medium, according to the manufacturer's instructions.

Metabolome analysis

Cells on DCCs were cultured at simulated microgravity or standard 1 × *g* for 24 h, washed with 5% (w/w) mannitol (Fujifilm Wako Pure Chemical Corporation), and incubated with methanol (Fujifilm Wako Pure Chemical Corporation) for 30 s. Subsequently, cells were incubated with 1 mM internal standard solution (Human Metabolome Technologies [HMT]) and collected in 1.5-ml tubes. The samples were centrifuged at 2,300 × g for 5 min at 4°C. The proteins were removed from the supernatant by ultrafiltration filters (HMT). Ionic metabolites were comprehensively measured at HMT using capillary electrophoresis time-of-flight mass spectrometry (CE-TOFMS) and capillary electrophoresis triple-quadrupole mass spectrometry (CE-QqQMS).

Accession numbers

The ribosome profiling and RNA-Seq data (GSE222998) obtained in this study were deposited in the National Center for Biotechnology Information (NCBI) Gene Expression Omnibus (GEO) database.

Figure and table legends

Figure 1. Genome-wide ribosome profiling reveals mitochondrial translation repression by microgravity in humans and nematodes.

(A and D) Schematic representation of experiments in the international space station (ISS) for HEK293 cells (A) and *C. elegans* (D). μg: microgravity.

(B) MA (M, log ratio; A, mean average) plots for ribosome footprint change (left), RNA abundance change (middle), and translation efficiency change (right) by 24-h microgravity (μg) culture in HEK293 cells. Significantly altered transcripts (false discovery rate [FDR] < 0.05) and mitochondrial genome-encoded mRNAs are highlighted.

(C) Box plots for ribosome footprint change (left), RNA abundance change (middle), and translation efficiency change (right) of mitochondrial genome-encoded mRNAs along the time course of microgravity culture.

(E) Cumulative distribution of ribosome footprint change (left), RNA abundance change (middle), and translation efficiency change (right) of nuclear genome-encoded mRNAs and mitochondrial genome-encoded mRNAs by 4 d of microgravity culture in *C. elegans*. The p value was calculated by the Mann–Whitney *U* test.

See also Figure S1.

Figure 2. Mitochondrial translation is a function of gravity.

(A) Schematic representation of experiments with a 3D clinostat to induce simulated microgravity (s-μg) in HEK293 cells.

(B) MA plots for ribosome footprint change (left), RNA abundance change (middle), and translation efficiency change (right) by 24 h of simulated microgravity culture in HEK293

cells. Significantly altered transcripts (false discovery rate [FDR] < 0.05) and mitochondrial genome-encoded mRNAs are highlighted.

(C) Box plots for ribosome footprint change (left), RNA abundance change (middle), and translation efficiency change (right) of mitochondrial genome-encoded mRNAs along the time course of simulated microgravity culture.

(D) On-gel FUNCAT experiments to monitor total and mitochondrial translation for the indicated cell lines and conditions. Cells were cultured in s-μ*g* for 24 h before cell harvest.

(E) On-gel FUNCAT experiments for mitochondrial translation in HEK293 ceslls. For the recovery experiments, cells were incubated at s-μ*g* for 24 h and then at 1 × *g* for 24 h.

(F) On-gel FUNCAT experiments to monitor total and mitochondrial translation for the indicated cell lines and conditions. Cells were cultured at 10 × *g* for 24 h before cell harvest.

For D-F, data from three replicates (points), the mean values (bars), and the s.d.s (errors) are shown. The p values were calculated by Student's t test (two-tailed) (D and F) and by the Tukey–Kramer test (two-tailed) (E).

See also Figure S2.

Figure 3. The attenuated laminin–integrin signal pathway causes mitochondrial translation repression in microgravity.

(A) Schematic representation of experiments to investigate the impacts of titrated cell adhesion mediated by laminin–integrin on mitochondrial translation.

(B) Relationship among laminin concentration for cell culture dish pretreatment, cell adhesion activity, and translation activity. For cell adhesion activity, the mean value

without laminin coating was set to "1". Total and mitochondrial protein synthesis were separately assayed. ρ, Spearman's rank correlation coefficient.

(C) On-gel FUNCAT experiments to monitor total and mitochondrial translation for the indicated cell lines and conditions. Dishes were pretreated with 0.25 μg/cm^2 laminin.

(D) On-gel FUNCAT experiments to monitor total and mitochondrial translation for the indicated cell lines and conditions. Cells were treated with 10 μg/ml RGDS peptide for 24 h.

(E) Box plots for ribosome footprint change (left), RNA abundance change (middle), and translation efficiency change (right) of mitochondria genome-encoded mRNAs along the time course of simulated microgravity culture with or without laminin treatment. Note that the data for no laminin treatment are the same as those in Figure 2C.

(F) Oxygen consumption rate (OCR) of HEK293 cells at base respiration and treated with oligomycin, carbonyl cyanide 4-(trifluoromethoxy)phenylhydrazone (FCCP), and rotenone/antimycin.

(G) Volcano plot for the metabolome changed by 24 h of simulated microgravity. TCA cycle-associated metabolites are highlighted.

For C and D, data from three replicates (points), the mean values (bars), and the s.d.s (errors) are shown. The p values were calculated by Student's t test (two-tailed).

For F, the mean values (points) from three replicates and the s.d.s (errors) are shown.

See also Figure S3.

Figure 4. The cellular pathway that transduces the signal from laminin–integrin cell adhesion to mitochondrial translation activation.

(A) On-gel FUNCAT experiments to monitor mitochondrial translation with siRNA transfection to knock down FAK.

(B, D, and F) On-gel FUNCAT experiments to monitor mitochondrial translation under treatment with the indicated compounds at the following concentrations for 12 h: NSC23766, 200 μM; ZCL278, 100 μM; Rhosin, 50 μM; BAY-293,1 μM; LY294002, 10 μM; SP600125, 20 μM; IPA-3, 5 μM; CK666, 25 μM; obatoclax, 2 μM; TW-37, 10 μM.

(C) Western blotting of RAC1 protein in the total cell lysate and in the GTP-bound fraction pulled down with the p21-binding domain (PBD) of PAK1. The quantified relative amount of RAC1 in the GTP-bound, activated form is shown.

(E) Western blotting of total PAK1 protein and the phosphorylated form (at S144 and S141). The quantified relative amount of phosphorylated PAK1 is shown.

(G) Western blotting of total BAD protein in the total lysate and in the mitochondria immunoprecipitated (IP) fraction with anti-TOM22 antibody.

(H) Representative distribution of Cy3-conjugated HPG signals normalized to AF647-labeled TOMM20 signals in the indicated cell lines (left). The dashed line presents the mean of the distribution. The quantification is shown on the right. The distribution of unnormalized Cy3-conjugated HPG signals and AF647-labeled TOMM20 signals are shown in Figure S4J.

(I) On-gel FUNCAT experiments to monitor mitochondrial translation in naïve and *BAD* KO HAP1 cells with a titrated concentration of laminin pretreatment.

For A-H, data from replicates (points, n = 3 for A, C, E, G, and H; n = 6 for B, D, and F), the mean values (bars), and the s.d.s (errors) are shown. The p values were calculated by Student's t test (two-tailed) (C, E, G, and H) and by the Tukey–Kramer test (two-tailed) (A, B, D, and F).

For I, data from three replicates and the mean values (bars) are shown.

See also Figure S4.

Figure 5. Minimized mechanical stress reduces mitochondrial translation.

(A) Schematic representation of experiments with minimized mechanical stress (MMS) in mouse hindlimb.

(B) MA plots for ribosome footprint change (left), RNA abundance change (middle), and translation efficiency change (right) by 14-d MMS in mouse soleus. Significantly altered transcripts (false discovery rate [FDR] < 0.05) and mitochondrial genome-encoded mRNAs are highlighted.

(C) Box plots for ribosome footprint change (left), RNA abundance change (middle), and translation efficiency change (right) of mitochondria genome-encoded mRNAs along the time course of MMS.

(D) Schematic representation of the model of gravitational and mechanical force-mediated mitochondrial translation activation.

See also Figure S5.

Figure S1. Characterization of ribosome profiling data in spaceflight samples. Related to Figure 1.

(A and I) The lengths of ribosome footprints in the indicated samples.

(B and J) Metagene plots of ribosome footprints relative to the start codon across the footprint length. The 5′ end positions of ribosome footprints are depicted. The color indicates read abundance. RPM, reads per million reads.

(C and K) Pearson's correlation coefficient (*r*) among the indicated samples in ribosome profiling and RNA-Seq. Black squares indicate the correlation of biological replicates.

(D and L) MA (M, log ratio; A, mean average) plots for ribosome footprint change (left), RNA abundance change (middle), and translation efficiency change (right) in HEK293 cells during 48 h of microgravity (μg) culture (D) and in *C. elegans* during 4 d of microgravity cultures (L). Significantly altered transcripts (false discovery rate [FDR] < 0.05) and mitochondrial genome-encoded mRNAs are highlighted.

(E and M) Gene Ontology (GO) analysis by DAVID (*72*, *73*) for genes downregulated or upregulated by microgravity. Color represents statistical significance, and circle size indicates the number of genes found in the GO category. The p values were calculated by a modified Fisher's exact test (EASE score).

(F and G) Box plots of ribosome footprint change (left), RNA abundance change (middle), and translation efficiency change (right) of nuclear genome-encoded OXPHOS subunits (F) and mitochondria-localized proteins (G) (defined by Mitocarta3 (*74*)) along the time course of microgravity culture of HEK293 cells.

(H) Box plots of the RNA abundance change (middle) of mtUPR target genes (defined by (*34*)) along the time course of microgravity culture of HEK293 cells.

Figure S2. Characterization of ribosome profiling data in HEK293 cells in simulated microgravity. Related to Figure 2.

(A) MA plots of ribosome footprint change (left), RNA abundance change (middle), and translation efficiency change (right) under 1 h of simulated microgravity culture in HEK293 cells. Significantly altered transcripts (false discovery rate [FDR] < 0.05) and mitochondrial genome-encoded mRNAs are highlighted.

(B and C) Box plots of ribosome footprint change (left), RNA abundance change (middle), and translation efficiency change (right) of nuclear-genome encoded OXPHOS subunits (B) and mitochondria localized proteins (C) (defined by Mitocarta3 (*74*)) along the time course of simulated microgravity culture of HEK293 cells.

(D and E) On-gel FUNCAT experiments to monitor total and mitochondrial translation for the indicated cell lines and conditions. Cells were cultured in s-μ*g* or 1 × *g* for 24 h before cell harvest.

(F and G) Relative mitochondrial DNA (mtDNA) content in the indicated cell lines and conditions. Cells were cultured in s-μ*g* or 10 × *g* for 24 h before cell harvest.

(H and I) Mitochondria in C2C12 cells were immunostained with AF647-labeled anti-TOMM20 antibody at the indicated culture conditions. Representative images of immunostaining (H) and quantification of the mitochondrial connected components (I) are shown. Scale bar, 20 μm.

(J) Box plots of the RNA abundance change (middle) of mtUPR target genes (defined by (*34*)) along the time course of simulated microgravity culture of HEK293 cells.

For D-G, data from three replicates (points), the mean values (bars), and the s.d.s (errors) are shown. The p values were calculated by Student's t test (two-tailed) (D).

Figure S3. Characterization of the phosphorylation status of FAK. Related to Figure 3.

(A, C, and E) Western blotting of total FAK protein and the phosphorylated form (at Y397). The quantified relative amount of phosphorylated FAK is shown.

(B) Relative ribosome footprint density (normalized to the average of ITGB1) of the indicated integrin subunit genes. Ribosome profiling data in HEK293 cells with 1 × *g* culture (Figure 2A) were used.

(D) On-gel FUNCAT experiments to monitor total and mitochondrial translation for the indicated cell lines and conditions. Dishes were pretreated with 0.25 μg/cm^2 laminin.

For A and C-E, data from three replicates (points), the mean values (bars), and the s.d.s (errors) are shown. The p values were calculated by Student's t test (two-tailed) (A, D, and E).

Figure S4. Characterization of chemical treatment for mitochondrial translation. Related to Figure 4.

(A) Western blotting of FAK protein after the knockdown experiments with siRNAs. β-Actin was used as the loading control. The quantified relative amount of FAK is shown.

(B) Schematic representation of the downstream signal transduction pathway of FAK to mitochondrial translation.

(C, E, and G) Relative cell viability with indicated compound treatments for 12 h. The reduction in cell viability under compound treatment showed the efficient blocks of the corresponding target protein's functions.

(D, F, H, and K) On-gel FUNCAT experiments to monitor mitochondrial translation in the absence of laminin precoating with the treatment of the indicated compounds for 12 h. We note that DMSO data in F were the same data for DMSO without laminin coating in Figure 4D.

(I) Western blotting of BAD protein in KO HAP1 cells. GAPDH was used as the loading control. The quantification of the relative amount of BAD is shown.

(J) Representative distribution of Cy3-conjugated HPG signals (left) and AF647-labeled TOMM20 signals (right) in the indicated cell lines. The dashed line presents the mean of the distribution.

(L and N) Representative distribution of the MitoTracker Green signal (left), the MitoTracker Red signal (middle), and the MitoTracker Green-normalized MitoTracker Red values (right) under the indicated conditions. Given that Mitotracker Red staining depends on membrane potential, the values normalized by Mitotracker Green, which standardizes the mitochondrial volumes in cells, represent relative membrane potential. The dashed line presents the mean of the distribution. HEK293 cells were treated with RGDS peptide for 24 h. Dishes were pretreated with 0.25 μg/cm^2 laminin. AU, arbitrary unit.

(M and O) Quantification of the relative membrane potential shown in L and N.

For A, C-I, K, M, and O, data from replicates (points, n = 3 for A, C, E, G, I, M, and O; n = 6 for D, F, and H: n =2 for K), the mean values (bars), and the s.d.s (errors) are shown. The p values were calculated by Student's t test (two-tailed) (I and O) and by the Tukey–Kramer test (two-tailed) (A, D, F, and H).

For C-H and K, cells were treated with the compounds at the following concentrations: NSC23766, 200 μM; ZCL278, 100 μM; Rhosin, 50 μM; BAY-293, 1 μM; LY294002, 10 μM; SP600125, 20 μM; IPA-3, 5 μM; CK666, 25 μM; obatoclax, 2 μM; TW-37, 10 μM; valinomycin, 2 μM.

Figure S5. Characterization of minimized mechanical stress treatment in mice. Related to Figure 5.

(A) Relative soleus muscle wet weight under the indicated conditions. Data were normalized to the mean value of age-matched mice without unloading treatment. The right and left knees served as different samples.

(B) On-gel FUNCAT experiments to monitor mitochondrial translation for the indicated cell lines and incubation time in s-μg before the cell harvest.

(C, F, and I) Relative cell viability with indicated compound treatment for 12 h. The reduced cell viability by compound treatment showed the efficient blocks of the corresponding target protein's functions.

(D, E, G, H, J, and K) On-gel FUNCAT experiments to monitor mitochondrial translation with the treatment of the indicated compounds for 12 h. Dishes were pretreated with 0.25 μg/cm^2 laminin. We note that the DMSO samples in D, G, and J were the data for DMSO without laminin coating, as in E, H, and K, respectively.

Data from replicates (points, n = 3 for B, C, D, E, F, and I; n = 6 for A, G, H, J, and K), the mean values (bars), and s.d.s (errors) are shown. The p values were calculated by Student's t test (two-tailed) (A) and by the Tukey–Kramer test (two-tailed) (B, G, H, and K).

For C-K, cells were treated with the compounds at the following concentrations: sorafenib, 1 μM; GW5074, 5 μM; ZM336372, 10 μM; venetoclax, 10 μM; A-1331852, 10 μM; S63845, 5 μM; 10 μM; BAI1, 1 μM; BTSA1, 20 μM; BAM7, 20 μM.

Table S1. A-site offsets for cytosolic and mitochondrial ribosome footprints. Related to Figures 1, 2, 3, and 5.

A-site offsets for cytoribosome footprints and mitoribosome footprints along the footprint length in ribosome profiling data obtained in this study are listed.

References

1. E. Afshinnekoo, R. T. Scott, M. J. MacKay, E. Pariset, E. Cekanaviciute, R. Barker, S. Gilroy, D. Hassane, S. M. Smith, S. R. Zwart, M. Nelman-Gonzalez, B. E. Crucian, S. A. Ponomarev, O. I. Orlov, D. Shiba, M. Muratani, M. Yamamoto, S. E. Richards, P. A. Vaishampayan, C. Meydan, J. Foox, J. Myrrhe, E. Istasse, N. Singh, K. Venkateswaran, J. A. Keune, H. E. Ray, M. Basner, J. Miller, M. H. Vitaterna, D. M. Taylor, D. Wallace, K. Rubins, S. M. Bailey, P. Grabham, S. V. Costes, C. E. Mason, A. Beheshti, Fundamental biological features of spaceflight: advancing the field to enable deep-space exploration. *Cell*. **183**, 1162–1184 (2020).

2. T. J. Goodwin, M. Christofidou-Solomidou, Oxidative stress and space biology: an organ-based approach. *Int. J. Mol. Sci.* **19**, 959 (2018).

3. W. A. da Silveira, H. Fazelinia, S. B. Rosenthal, E. C. Laiakis, M. S. Kim, C. Meydan, Y. Kidane, K. S. Rathi, S. M. Smith, B. Stear, Y. Ying, Y. Zhang, J. Foox, S. Zanello, B. Crucian, D. Wang, A. Nugent, H. A. Costa, S. R. Zwart, S. Schrepfer, R. A. L. Elworth, N. Sapoval, T. Treangen, M. MacKay, N. S. Gokhale, S. M. Horner, L. N. Singh, D. C. Wallace, J. S. Willey, J. C. Schisler, R. Meller, J. T. McDonald, K. M. Fisch, G. Hardiman, D. Taylor, C. E. Mason, S. V. Costes, A. Beheshti, Comprehensive multi-omics analysis reveals mitochondrial stress as a central biological hub for spaceflight impact. *Cell*. **183**, 1185–1201.e20 (2020).

4. R. Zhang, H.-H. Ran, L.-L. Cai, L. Zhu, J.-F. Sun, L. Peng, X.-J. Liu, L.-N. Zhang, Z. Fang, Y.-Y. Fan, G. Cui, Simulated microgravity-induced mitochondrial dysfunction in rat cerebral arteries. *FASEB J.* **28**, 2715–2724 (2014).

5. F. E. Garrett-Bakelman, M. Darshi, S. J. Green, R. C. Gur, L. Lin, B. R. Macias, M. J. McKenna, C. Meydan, T. Mishra, J. Nasrini, B. D. Piening, L. F. Rizzardi, K. Sharma, J. H. Siamwala, L. Taylor, M. H. Vitaterna, M. Afkarian, E. Afshinnekoo, S. Ahadi, A. Ambati, M. Arya, D. Bezdan, C. M. Callahan, S. Chen, A. M. K. Choi, G. E. Chlipala, K. Contrepois, M. Covington, B. E. Crucian, I. De Vivo, D. F. Dinges, D. J. Ebert, J. I. Feinberg, J. A. Gandara, K. A. George, J. Goutsias, G. S. Grills, A. R. Hargens, M. Heer, R. P. Hillary, A. N. Hoofnagle, V. Y. H. Hook, G. Jenkinson, P. Jiang, A. Keshavarzian, S. S. Laurie, B. Lee-McMullen, S. B. Lumpkins, M. MacKay, M. G. Maienschein-Cline, A. M. Melnick, T. M. Moore, K. Nakahira, H. H. Patel, R. Pietrzyk, V. Rao, R. Saito, D. N. Salins, J. M. Schilling, D. D. Sears, C. K. Sheridan, M. B. Stenger, R. Tryggvadottir, A. E. Urban, T. Vaisar, B. Van Espen, J. Zhang, M. G. Ziegler, S. R. Zwart, J. B. Charles, C. E. Kundrot, G. B. I. Scott, S. M. Bailey, M. Basner, A. P. Feinberg, S. M. C. Lee, C. E. Mason, E. Mignot, B. K. Rana, S. M. Smith, M. P. Snyder, F. W. Turek, The NASA twins study: a multidimensional analysis of a year-long human spaceflight. *Science*. **364**, eaau8650 (2019).

6. A. Adrian, K. Schoppmann, J. Sromicki, S. Brungs, M. von der Wiesche, B. Hock, W. Kolanus, R. Hemmersbach, O. Ullrich, The oxidative burst reaction in mammalian cells depends on gravity. *Cell Commun. Signal.* **11**, 98 (2013).

7. S. Ray, S. Gebre, H. Fogle, D. C. Berrios, P. B. Tran, J. M. Galazka, S. V. Costes, GeneLab: Omics database for spaceflight experiments. *Bioinformatics*. **35**, 1753–1759 (2019).

8. D. C. Berrios, J. Galazka, K. Grigorev, S. Gebre, S. V. Costes, NASA GeneLab: interfaces for the exploration of space omics data. *Nucleic Acids Res.* **49**, D1515–D1522 (2021).

9. A. Higashibata, T. Hashizume, K. Nemoto, N. Higashitani, T. Etheridge, C. Mori, S. Harada, T. Sugimoto, N. J. Szewczyk, S. A. Baba, Others, Microgravity elicits reproducible alterations in cytoskeletal and metabolic gene and protein expression in space-flown *Caenorhabditis elegans*. *npj Microgravity*. **2**, 1–8 (2016).

10. K. R. Jonscher, A. Alfonso-Garcia, J. L. Suhalim, D. J. Orlicky, E. O. Potma, V. L. Ferguson, M. L. Bouxsein, T. A. Bateman, L. S. Stodieck, M. Levi, J. E. Friedman, D. S. Gridley, M. J. Pecaut, Spaceflight activates lipotoxic pathways in mouse liver. *PLoS One*. **11**, e0152877 (2016).

11. A. Beheshti, E. Cekanaviciute, D. J. Smith, S. V. Costes, Global transcriptomic analysis suggests carbon dioxide as an environmental stressor in spaceflight: A systems biology GeneLab case study. *Sci. Rep.* **8**, 4191 (2018).

12. A. Beheshti, K. Chakravarty, H. Fogle, H. Fazelinia, W. A. da Silveira, V. Boyko, S.-H. L. Polo, A. M. Saravia-Butler, G. Hardiman, D. Taylor, J. M. Galazka, S. V. Costes, Multi-omics analysis of multiple missions to space reveal a theme of lipid dysregulation in mouse liver. *Sci. Rep.* **9**, 19195 (2019).

13. E. G. Overbey, W. A. da Silveira, S. Stanbouly, N. C. Nishiyama, G. D. Roque-Torres, M. J. Pecaut, D. C. Zawieja, C. Wang, J. S. Willey, M. D. Delp, G. Hardiman, X. W. Mao, Spaceflight influences gene expression, photoreceptor integrity, and oxidative stress-related damage in the murine retina. *Sci. Rep.* **9**, 13304 (2019).

14. M. L. Gertz, C. R. Chin, D. Tomoiaga, M. MacKay, C. Chang, D. Butler, E. Afshinnekoo, D. Bezdan, M. A. Schmidt, C. Mozsary, A. Melnick, F. Garrett-Bakelman, B. Crucian, S. M. C. Lee, S. R. Zwart, S. M. Smith, C. Meydan, C. E. Mason, Multi-omic, single-cell, and biochemical profiles of astronauts guide pharmacological strategies for returning to gravity. *Cell Rep.* **33**, 108429 (2020).

15. D. Bezdan, K. Grigorev, C. Meydan, F. A. Pelissier Vatter, M. Cioffi, V. Rao, M. MacKay, K. Nakahira, P. Burnham, E. Afshinnekoo, C. Westover, D. Butler, C. Mozsary, T. Donahoe, J. Foox, T. Mishra, S. Lucotti, B. K. Rana, A. M. Melnick, H. Zhang, I. Matei, D. Kelsen, K. Yu, D. C. Lyden, L. Taylor, S. M. Bailey, M. P. Snyder, F. E. Garrett-Bakelman, S. Ossowski, I. De Vlaminck, C. E. Mason, Cell-free DNA (cfDNA) and exosome profiling from a year-long human spaceflight reveals circulating biomarkers. *iScience*. **23**, 101844 (2020).

16. A. Higashitani, T. Hashizume, M. Takiura, N. Higashitani, M. Teranishi, R.

Oshima, S. Yano, K. Kuriyama, A. Higashibata, Histone deacetylase HDA-4-mediated epigenetic regulation in space-flown *C. elegans*. *npj Microgravity*. **7**, 33 (2021).

17. S. D. Mhatre, J. Iyer, J. Petereit, R. M. Dolling-Boreham, A. Tyryshkina, A. M. Paul, R. Gilbert, M. Jensen, R. J. Woolsey, S. Anand, M. B. Sowa, D. R. Quilici, S. V. Costes, S. Girirajan, S. Bhattacharya, Artificial gravity partially protects space-induced neurological deficits in *Drosophila melanogaster*. *Cell Rep.* **40**, 111279 (2022).

18. G. Vitry, R. Finch, G. Mcstay, A. Behesti, S. Déjean, T. Larose, V. Wotring, W. A. da Silveira, Muscle atrophy phenotype gene expression during spaceflight is linked to a metabolic crosstalk in both the liver and the muscle in mice. *iScience*. **25**, 105213 (2022).

19. T. Pan, Adaptive translation as a mechanism of stress response and adaptation. *Annu. Rev. Genet.* **47**, 121–137 (2013).

20. P. P. Roux, I. Topisirovic, Signaling pathways involved in the regulation of mRNA translation. *Mol. Cell. Biol.* **38**, e00070–18 (2018).

21. V. M. Advani, P. Ivanov, Translational control under stress: reshaping the translatome. *Bioessays*. **41**, e1900009 (2019).

22. M. Costa-Mattioli, P. Walter, The integrated stress response: from mechanism to disease. *Science*. **368**, eaat5314 (2020).

23. M. Mito, Y. Shichino, S. Iwasaki, Thor-Ribo-Seq: ribosome profiling tailored for low input with RNA-dependent RNA amplification. *bioRxiv* (2023), doi:10.1101/2023.01.15.524129.

24. S. Iwasaki, S. N. Floor, N. T. Ingolia, Rocaglates convert DEAD-box protein eIF4A into a sequence-selective translational repressor. *Nature*. **534**, 558–561 (2016).

25. K. Kashiwagi, Y. Shichino, T. Osaki, A. Sakamoto, M. Nishimoto, M. Takahashi, M. Mito, F. Weber, Y. Ikeuchi, S. Iwasaki, T. Ito, eIF2B-capturing viral protein NSs suppresses the integrated stress response. *Nat. Commun.* **12**, 1–12 (2021).

26. X. Zhang, X. Zuo, B. Yang, Z. Li, Y. Xue, Y. Zhou, J. Huang, X. Zhao, J. Zhou, Y. Yan, H. Zhang, P. Guo, H. Sun, L. Guo, Y. Zhang, X. D. Fu, MicroRNA directly enhances mitochondrial translation during muscle differentiation. *Cell*. **158**, 607–619 (2014).

27. R. Yousefi, E. F. Fornasiero, L. Cyganek, J. Montoya, S. Jakobs, S. O. Rizzoli, P. Rehling, D. Pacheu-Grau, Monitoring mitochondrial translation in living cells. *EMBO Rep.* **22**, e51635 (2021).

28. M. Zorkau, C. A. Albus, R. Berlinguer-Palmini, Z. M. A. Chrzanowska-

Lightowlers, R. N. Lightowlers, High-resolution imaging reveals compartmentalization of mitochondrial protein synthesis in cultured human cells. *Proc. Natl. Acad. Sci. U. S. A.* **118**, e2008778118 (2021).

29. Y. Kimura, H. Saito, T. Osaki, Y. Ikegami, T. Wakigawa, Y. Ikeuchi, S. Iwasaki, Mito-FUNCAT-FACS reveals cellular heterogeneity in mitochondrial translation. *RNA*. **28**, 895–904 (2022).

30. A. Apostolopoulos, S. Iwasaki, Into the matrix: current methods for mitochondrial translation studies. *J. Biochem.* **171**, 379–387 (2022).

31. S. Wu, F. Zhou, Z. Zhang, D. Xing, Mitochondrial oxidative stress causes mitochondrial fragmentation via differential modulation of mitochondrial fission-fusion proteins. *FEBS J.* **278**, 941–954 (2011).

32. H.-G. Sprenger, T. Langer, The good and the bad of mitochondrial breakups. *Trends Cell Biol.* **29**, 888–900 (2019).

33. C. Münch, The different axes of the mammalian mitochondrial unfolded protein response. *BMC Biol.* **16**, 81 (2018).

34. T. Shpilka, C. M. Haynes, The mitochondrial UPR: mechanisms, physiological functions and implications in ageing. *Nat. Rev. Mol. Cell Biol.* **19**, 109–120 (2018).

35. X. Tan, A. Xu, T. Zhao, Q. Zhao, J. Zhang, C. Fan, Y. Deng, A. Freywald, H. Genth, J. Xiang, Simulated microgravity inhibits cell focal adhesions leading to reduced melanoma cell proliferation and metastasis via FAK/RhoA-regulated mTORC1 and AMPK pathways. *Sci. Rep.* **8**, 3769 (2018).

36. J. Bauer, Microgravity and cell adherence. *Int. J. Mol. Sci.* **21**, 2214 (2020).

37. X. Lin, K. Zhang, D. Wei, Y. Tian, Y. Gao, Z. Chen, A. Qian, The impact of spaceflight and simulated microgravity on cell adhesion. *Int. J. Mol. Sci.* **21**, 3031 (2020).

38. R. Nishiuchi, J. Takagi, M. Hayashi, H. Ido, Y. Yagi, N. Sanzen, T. Tsuji, M. Yamada, K. Sekiguchi, Ligand-binding specificities of laminin-binding integrins: A comprehensive survey of laminin–integrin interactions using recombinant α3β1, α6β1, α7β1 and α6β4 integrins. *Matrix Biol.* **25**, 189–197 (2006).

39. M. Takizawa, T. Arimori, Y. Taniguchi, Y. Kitago, E. Yamashita, J. Takagi, K. Sekiguchi, Mechanistic basis for the recognition of laminin-511 by α6β1 integrin. *Sci Adv*. **3**, e1701497 (2017).

40. S. K. Mitra, D. A. Hanson, D. D. Schlaepfer, Focal adhesion kinase: in command and control of cell motility. *Nat. Rev. Mol. Cell Biol.* **6**, 56–68 (2005).

41. F. J. Sulzmaier, C. Jean, D. D. Schlaepfer, FAK in cancer: mechanistic findings and clinical applications. *Nat. Rev. Cancer*. **14**, 598–610 (2014).

42. H. K. Bid, R. D. Roberts, P. K. Manchanda, P. J. Houghton, RAC1: an emerging therapeutic option for targeting cancer angiogenesis and metastasis. *Mol. Cancer Ther.* **12**, 1925–1934 (2013).

43. R. Kumar, A. E. Gururaj, C. J. Barnes, p21-activated kinases in cancer. *Nat. Rev. Cancer*. **6**, 459–471 (2006).

44. M. Radu, G. Semenova, R. Kosoff, J. Chernoff, PAK signalling during the development and progression of cancer. *Nat. Rev. Cancer*. **14**, 13–25 (2014).

45. D. Yao, C. Li, M. S. R. Rajoka, Z. He, J. Huang, J. Wang, J. Zhang, p21-activated kinase 1: emerging biological functions and potential therapeutic targets in cancer. *Theranostics*. **10**, 9741–9766 (2020).

46. D. Z. Ye, S. Jin, Y. Zhuo, J. Field, p21-activated kinase 1 (Pak1) phosphorylates BAD directly at serine 111 in vitro and indirectly through Raf-1 at serine 112. *PLoS One*. **6**, e27637 (2011).

47. J. E. Chipuk, T. Moldoveanu, F. Llambi, M. J. Parsons, D. R. Green, The BCL-2 family reunion. *Mol. Cell*. **37**, 299–310 (2010).

48. P. E. Czabotar, G. Lessene, A. Strasser, J. M. Adams, Control of apoptosis by the BCL-2 protein family: implications for physiology and therapy. *Nat. Rev. Mol. Cell Biol.* **15**, 49–63 (2014).

49. A. Ashkenazi, W. J. Fairbrother, J. D. Leverson, A. J. Souers, From basic apoptosis discoveries to advanced selective BCL-2 family inhibitors. *Nat. Rev. Drug Discov.* **16**, 273–284 (2017).

50. C. Côté, D. Boulet, J. Poirier, Expression of the mammalian mitochondrial genome. Role for membrane potential in the production of mature translation products. *J. Biol. Chem.* **265**, 7532–7538 (1990).

51. U. Richter, T. Lahtinen, P. Marttinen, F. Suomi, B. J. Battersby, Quality control of mitochondrial protein synthesis is required for membrane integrity and cell fitness. *J. Cell Biol.* **211**, 373–389 (2015).

52. L. D. Cruz-Zaragoza, S. Dennerlein, A. Linden, R. Yousefi, E. Lavdovskaia, A. Aich, R. R. Falk, R. Gomkale, T. Schöndorf, M. T. Bohnsack, R. Richter-Dennerlein, H. Urlaub, P. Rehling, An *in vitro* system to silence mitochondrial gene expression. *Cell*. **184**, 5824–5837.e15 (2021).

53. M. T. Couvillion, I. C. Soto, G. Shipkovenska, L. S. Churchman, Synchronized mitochondrial and cytosolic translation programs. *Nature*. **533**, 499–503 (2016).

54. I. Soto, M. Couvillion, K. G. Hansen, E. McShane, J. C. Moran, A. Barrientos, L. S. Churchman, Balanced mitochondrial and cytosolic translatomes underlie the biogenesis of human respiratory complexes. *Genome Biol.* **23**, 170 (2022).

55. N. Wang, J. P. Butler, D. E. Ingber, Mechanotransduction across the cell surface and through the cytoskeleton. *Science*. **260**, 1124–1127 (1993).

56. D. T. Butcher, T. Alliston, V. M. Weaver, A tense situation: forcing tumour progression. *Nat. Rev. Cancer*. **9**, 108–122 (2009).

57. N. Wang, Cellular adhesion: instant integrin mechanosensing. *Nat. Mater.* **16**, 1173–1174 (2017).

58. N. Strohmeyer, M. Bharadwaj, M. Costell, R. Fässler, D. J. Müller, Fibronectin-bound α5β1 integrins sense load and signal to reinforce adhesion in less than a second. *Nat. Mater.* **16**, 1262–1270 (2017).

59. S. E. Gordon, M. Flück, F. W. Booth, Selected Contribution: Skeletal muscle focal adhesion kinase, paxillin, and serum response factor are loading dependent. *J. Appl. Physiol.* **90**, 1174–1183 (2001).

60. T. Nikawa, K. Ishidoh, K. Hirasaka, I. Ishihara, M. Ikemoto, M. Kano, E. Kominami, I. Nonaka, T. Ogawa, G. R. Adams, K. M. Baldwin, N. Yasui, K. Kishi, S. 'ichi Takeda, Skeletal muscle gene expression in space-flown rats. *FASEB J.* **18**, 522–524 (2004).

61. M. E. Chicurel, R. H. Singer, C. J. Meyer, D. E. Ingber, Integrin binding and mechanical tension induce movement of mRNA and ribosomes to focal adhesions. *Nature*. **392**, 730–733 (1998).

62. J. Chung, T. H. Kim, Integrin-dependent translational control: implication in cancer progression. *Microsc. Res. Tech.* **71**, 380–386 (2008).

63. M. Willett, H. J. Pollard, M. Vlasak, S. J. Morley, Localization of ribosomes and translation initiation factors to talin/beta3-integrin-enriched adhesion complexes in spreading and migrating mammalian cells. *Biol. Cell*. **102**, 265–276 (2010).

64. N. Tanigawa, S. Yano, A. Higashibata, Y. Tsuchiya, H. Tanii, N. Ando, K. Kubota, M. Nagase, Development and validation of a closed chamber for cell culture experiments in space. *Biological Sciences in Space*. **28**, 1–5 (2014).

65. S. Yano, D. Masuda, H. Kasahara, K. Omori, A. Higashibata, M. Asashima, T. Ohnishi, F. Yatagai, S. Kamisaka, T. Furusawa, A. Higashitani, H. J. Majima, T. Nikawa, K. Wakabayashi, H. Takahashi, H. Suzuki, T. Shimazu, K. Fukui, A. Hattori, F. Tanigaki, M. Shirakawa, T. Nakamura, Y. Yoshimura, N. Suzuki, N. Ishioka, Excellent thermal control ability of Cell Biology Experiment Facility (CBEF) for ground-based experiments and experiments onboard the Kibo Japanese experiment module of International Space Station. *Biological Sciences in Space*. **26**, 12–20 (2012).

66. M. Mito, Y. Mishima, S. Iwasaki, Protocol for disome profiling to survey ribosome collision in humans and zebrafish. *STAR Protoc*. **1**, 100168 (2020).

67. N. J. McGlincy, N. T. Ingolia, Transcriptome-wide measurement of translation by ribosome profiling. *Methods*. **126**, 112–129 (2017).

68. S. Chen, Y. Zhou, Y. Chen, J. Gu, fastp: an ultra-fast all-in-one FASTQ preprocessor. *Bioinformatics*. **34**, i884–i890 (2018).

69. A. Dobin, C. A. Davis, F. Schlesinger, J. Drenkow, C. Zaleski, S. Jha, P. Batut, M. Chaisson, T. R. Gingeras, STAR: ultrafast universal RNA-seq aligner. *Bioinformatics*. **29**, 15–21 (2013).

70. T. Smith, A. Heger, I. Sudbery, UMI-tools: modeling sequencing errors in Unique Molecular Identifiers to improve quantification accuracy. *Genome Res.* **27**, 491–499 (2017).

71. M. I. Love, W. Huber, S. Anders, Moderated estimation of fold change and dispersion for RNA-seq data with DESeq2. *Genome Biol.* **15**, 550 (2014).

72. D. W. Huang, B. T. Sherman, R. A. Lempicki, Systematic and integrative analysis of large gene lists using DAVID bioinformatics resources. *Nat. Protoc.* **4**, 44–57 (2009).

73. D. W. Huang, B. T. Sherman, R. A. Lempicki, Bioinformatics enrichment tools: paths toward the comprehensive functional analysis of large gene lists. *Nucleic Acids Res.* **37**, 1–13 (2009).

74. S. Rath, R. Sharma, R. Gupta, T. Ast, C. Chan, T. J. Durham, R. P. Goodman, Z. Grabarek, M. E. Haas, W. H. W. Hung, P. R. Joshi, A. A. Jourdain, S. H. Kim, A. V. Kotrys, S. S. Lam, J. G. McCoy, J. D. Meisel, M. Miranda, A. Panda, A. Patgiri, R. Rogers, S. Sadre, H. Shah, O. S. Skinner, T.-L. To, M. A. Walker, H. Wang, P. S. Ward, J. Wengrod, C.-C. Yuan, S. E. Calvo, V. K. Mootha, MitoCarta3.0: an updated mitochondrial proteome now with sub-organelle localization and pathway annotations. *Nucleic Acids Res.* **49**, D1541–D1547 (2020).

75. T. Kitami, D. J. Logan, J. Negri, T. Hasaka, N. J. Tolliday, A. E. Carpenter, B. M. Spiegelman, V. K. Mootha, A chemical screen probing the relationship between mitochondrial content and cell size. *PLoS One*. **7**, e33755 (2012).

76. S. M. Rafelski, M. P. Viana, Y. Zhang, Y.-H. M. Chan, K. S. Thorn, P. Yam, J. C. Fung, H. Li, L. da F. Costa, W. F. Marshall, Mitochondrial network size scaling in budding yeast. *Science*. **338**, 822–824 (2012).

77. M. P. Viana, S. Lim, S. M. Rafelski, Quantifying mitochondrial content in living cells. *Methods Cell Biol.* **125**, 77–93 (2015).

78. Q. Fang, Y. Kimura, T. Shimazu, T. Suzuki, A. Yamada, N. Dohmae, S. Iwasaki, Y. Shinkai, Mammalian HEMK1 methylates glutamine residue of the GGQ motif of mitochondrial release factors. *Sci. Rep.* **12**, 4104 (2022).

79. Y. Shichino, M. Mito, K. Kashiwagi, M. Takahashi, T. Ito, N. T. Ingolia, S. Iwasaki, A specific eIF4A paralog facilitates LARP1-mediated translation repression during mTORC1 inhibition. *bioRxiv* (2021), doi:10.1101/2021.09.18.460932.

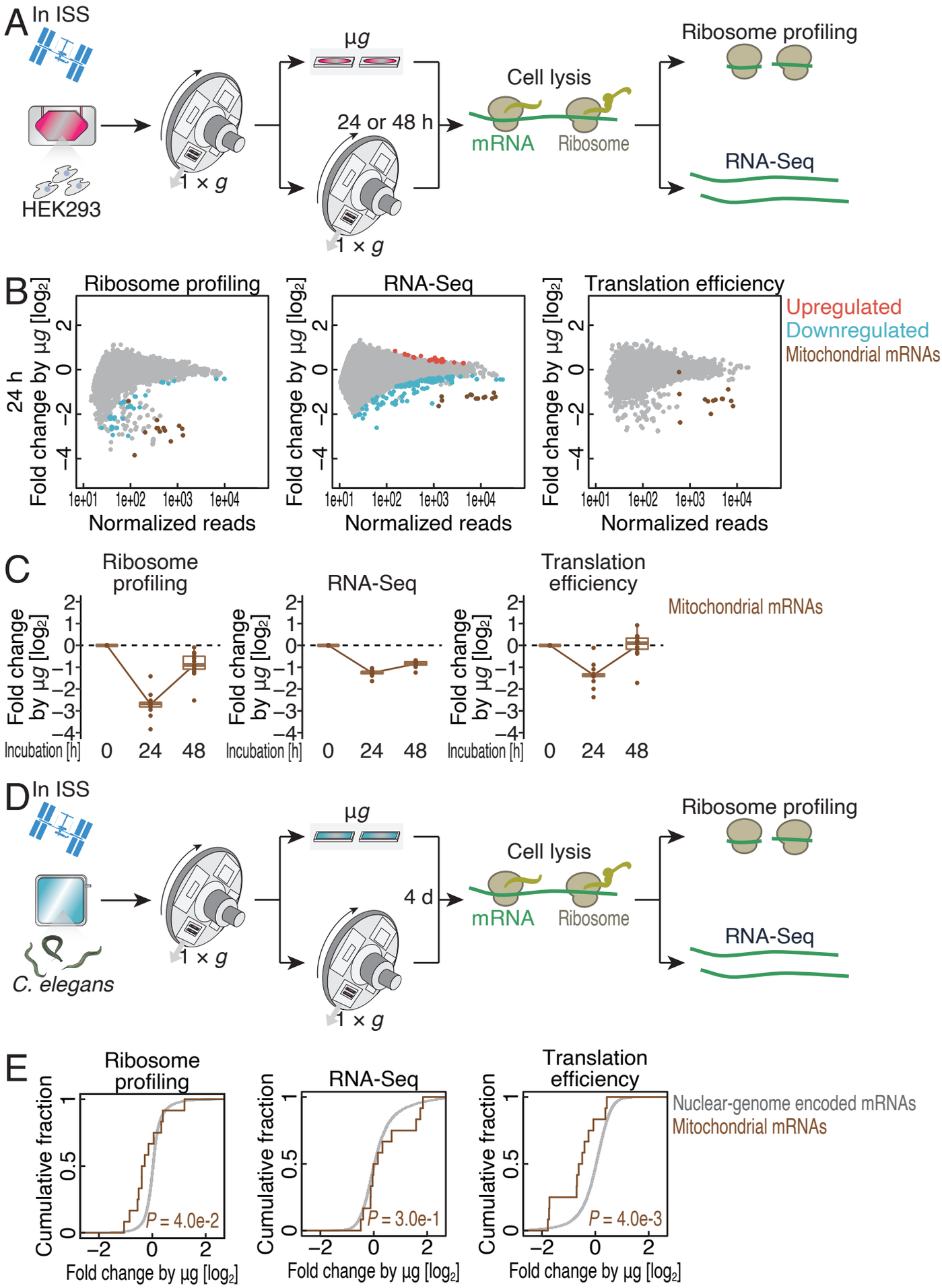

Figure 1 Wakigawa, Kimura *et al.* (2023)

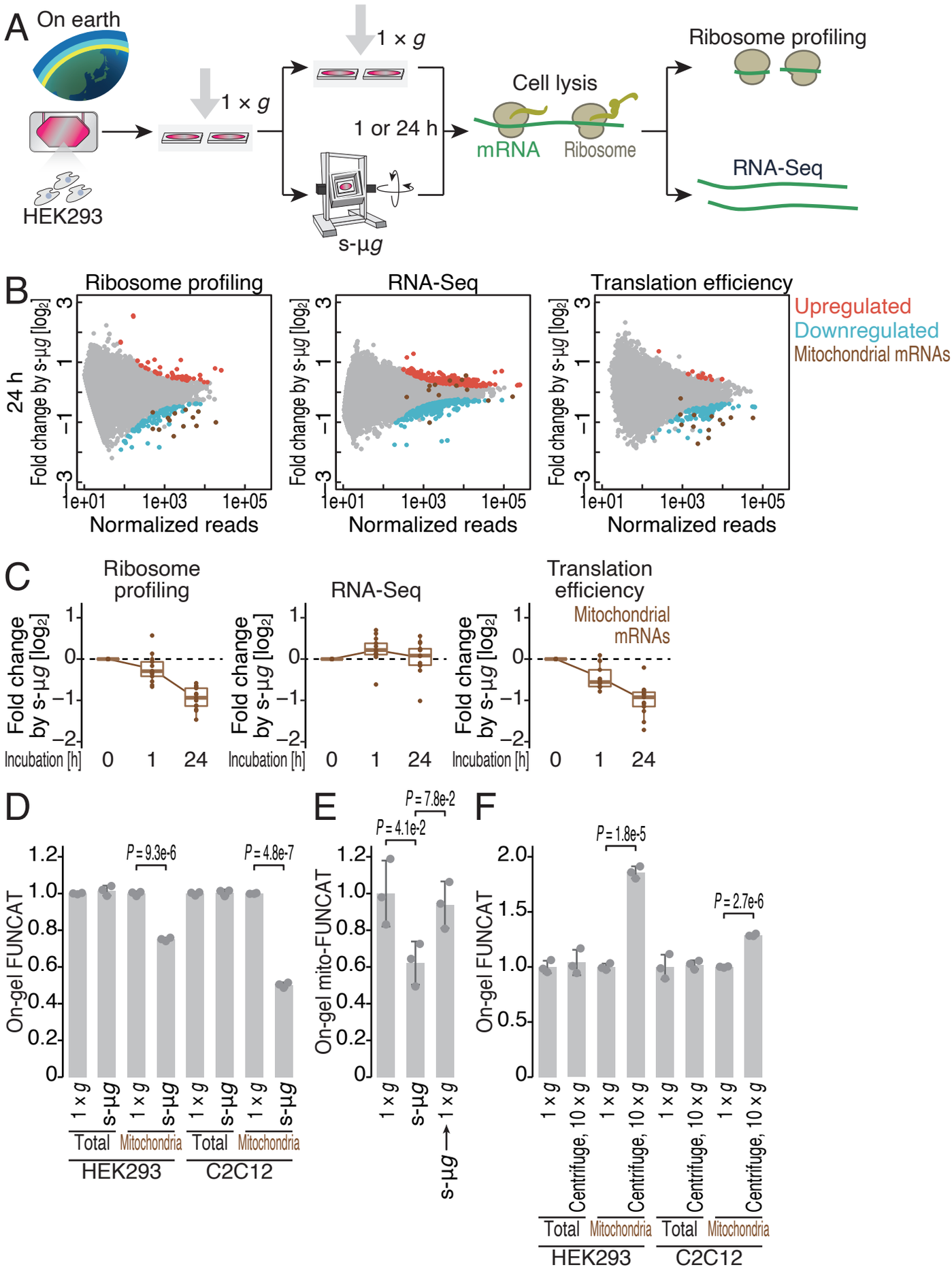

Figure 2 Wakigawa, Kimura *et al.* (2023)

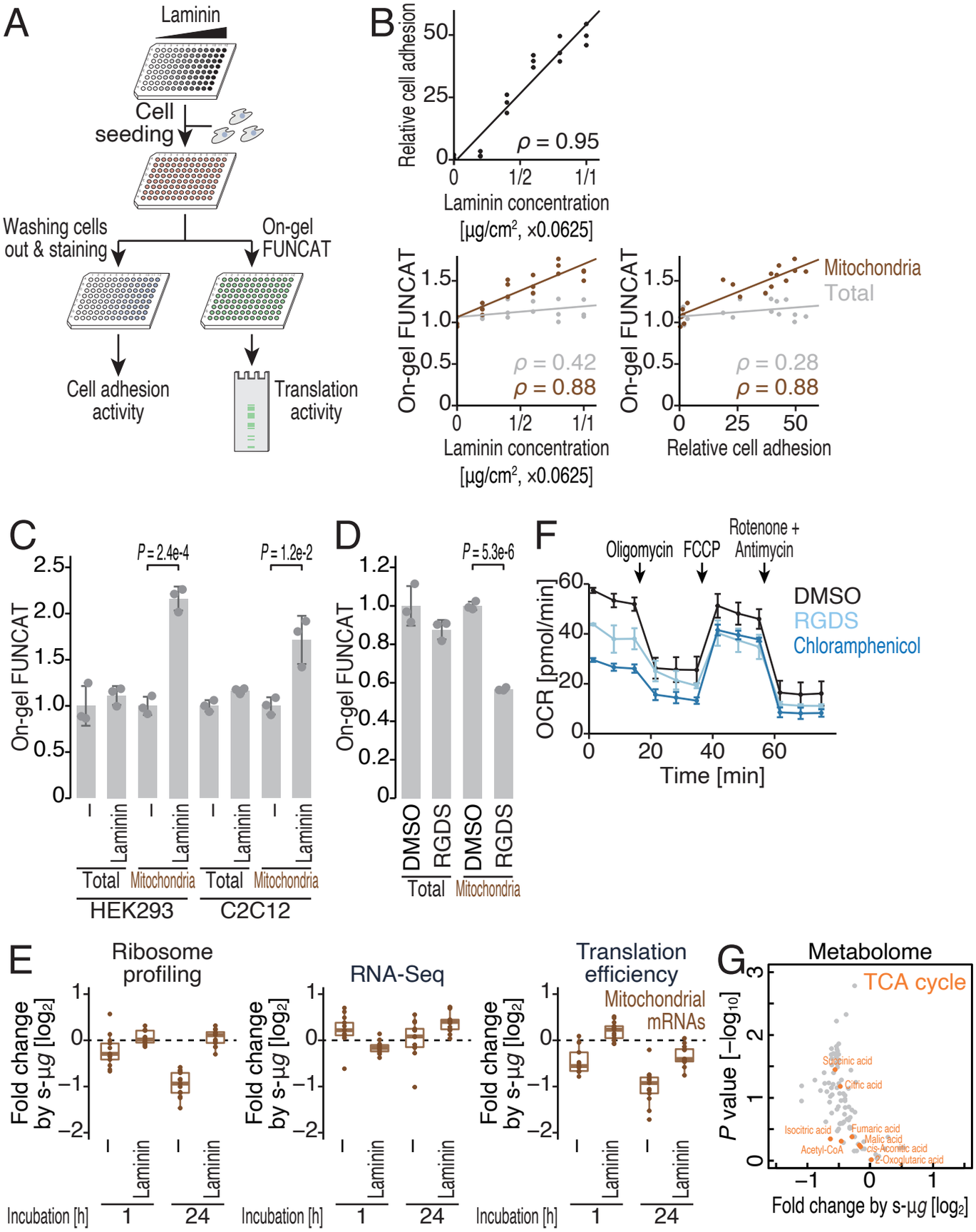

Figure 3 Wakigawa, Kimura *et al.* (2023)

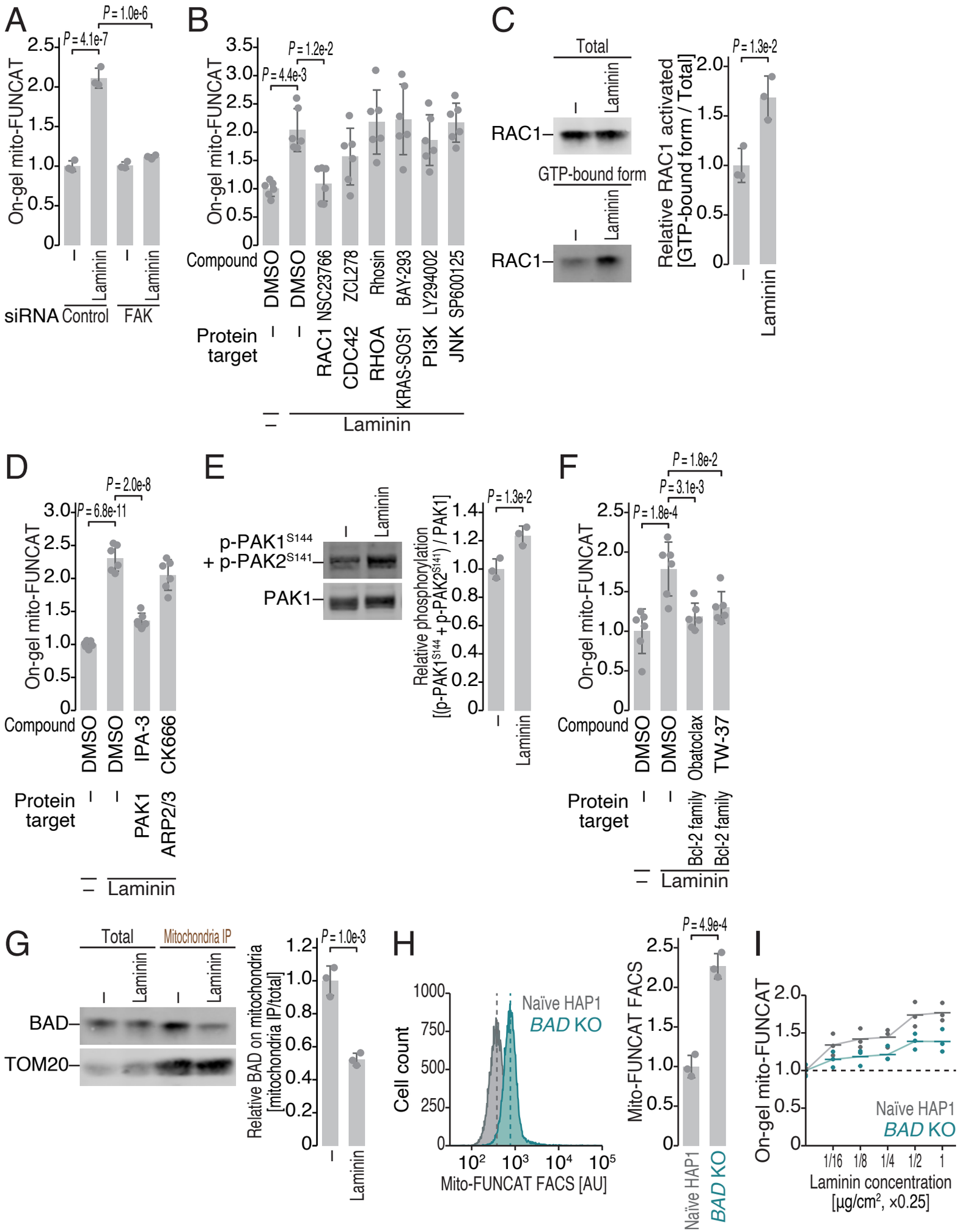

Figure 4 Wakigawa, Kimura *et al.* (2023)

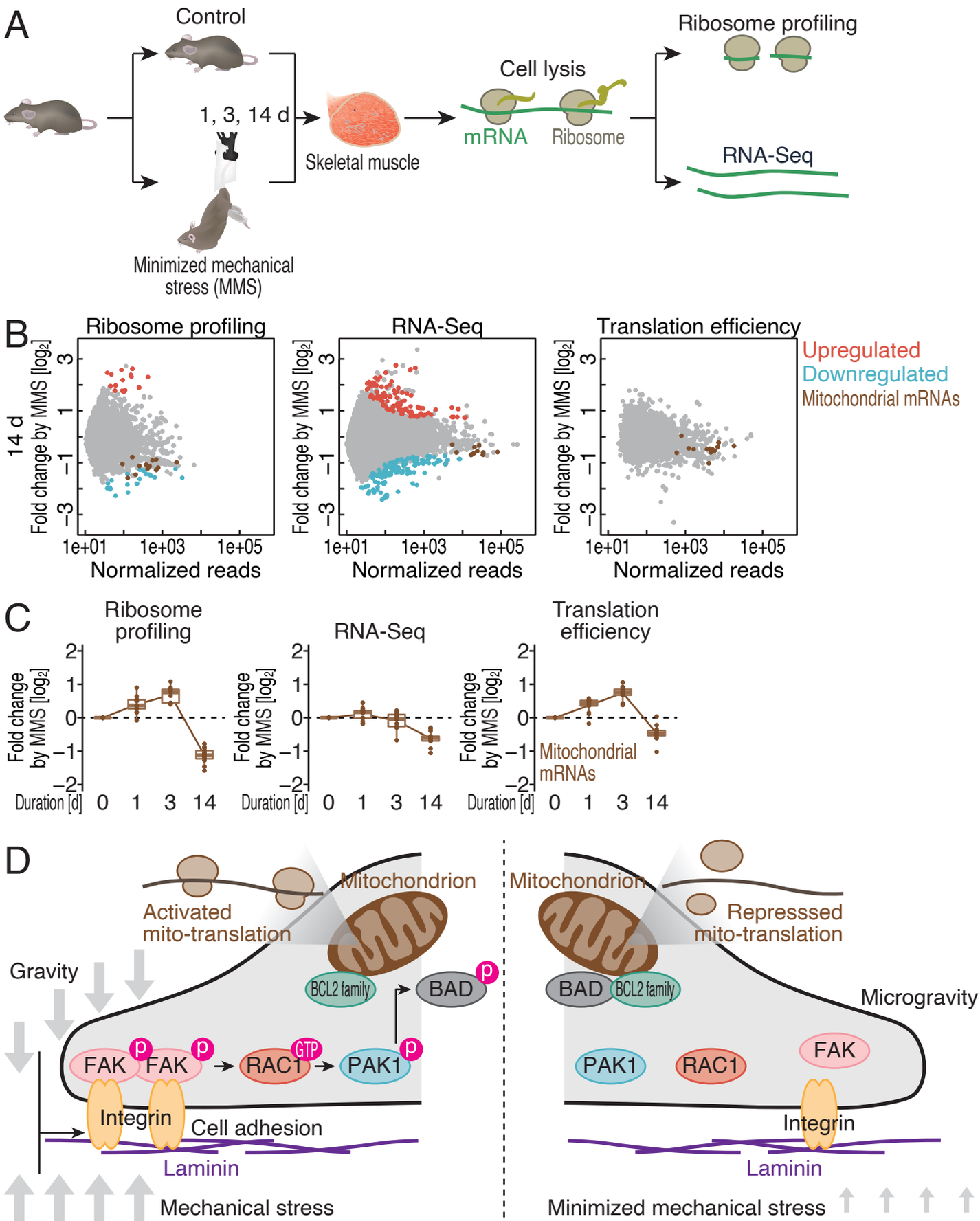

Figure 5 Wakigawa, Kimura *et al.* (2023)

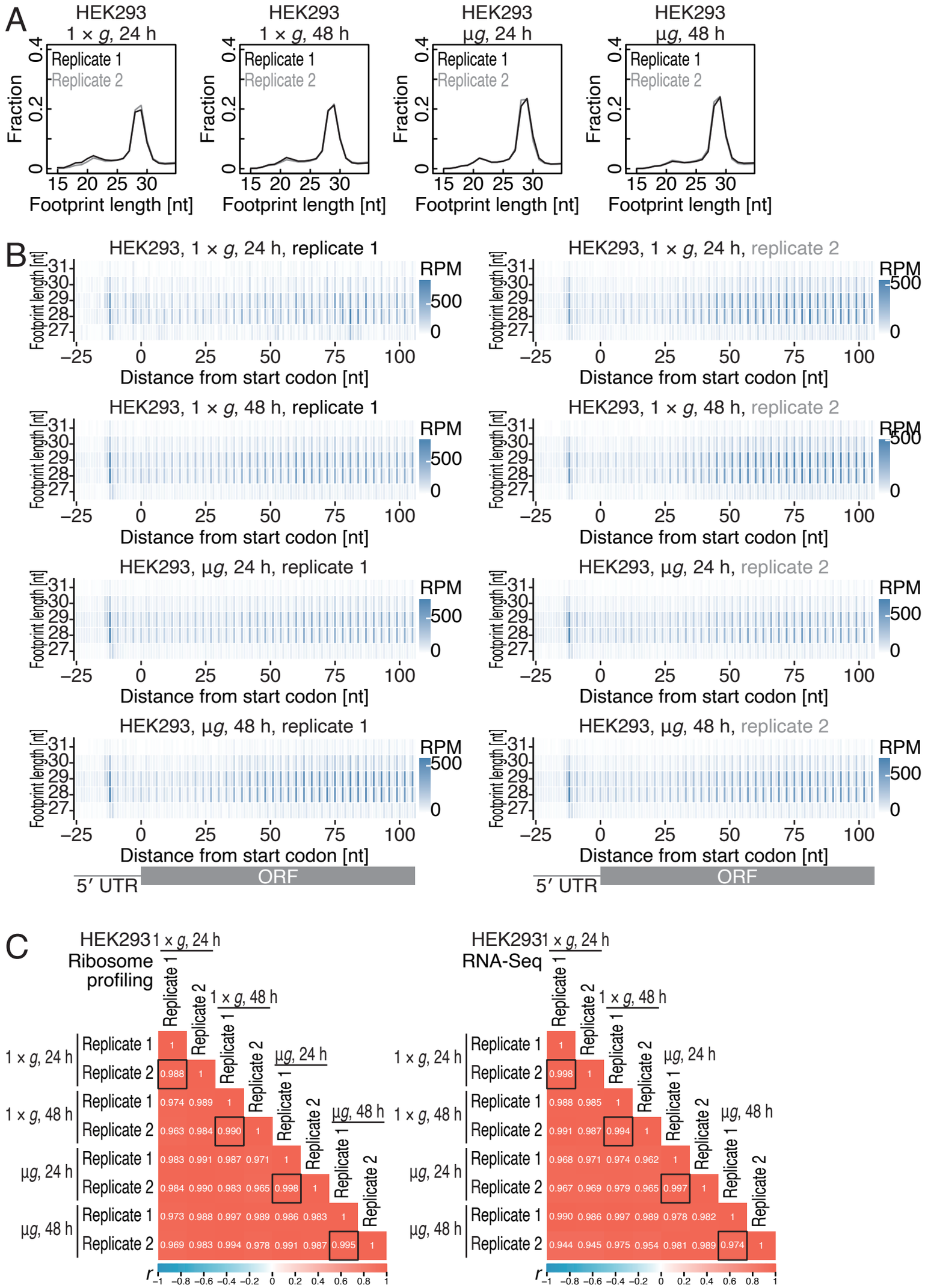

Figure S1 Wakigawa, Kimura *et al.* (2023)

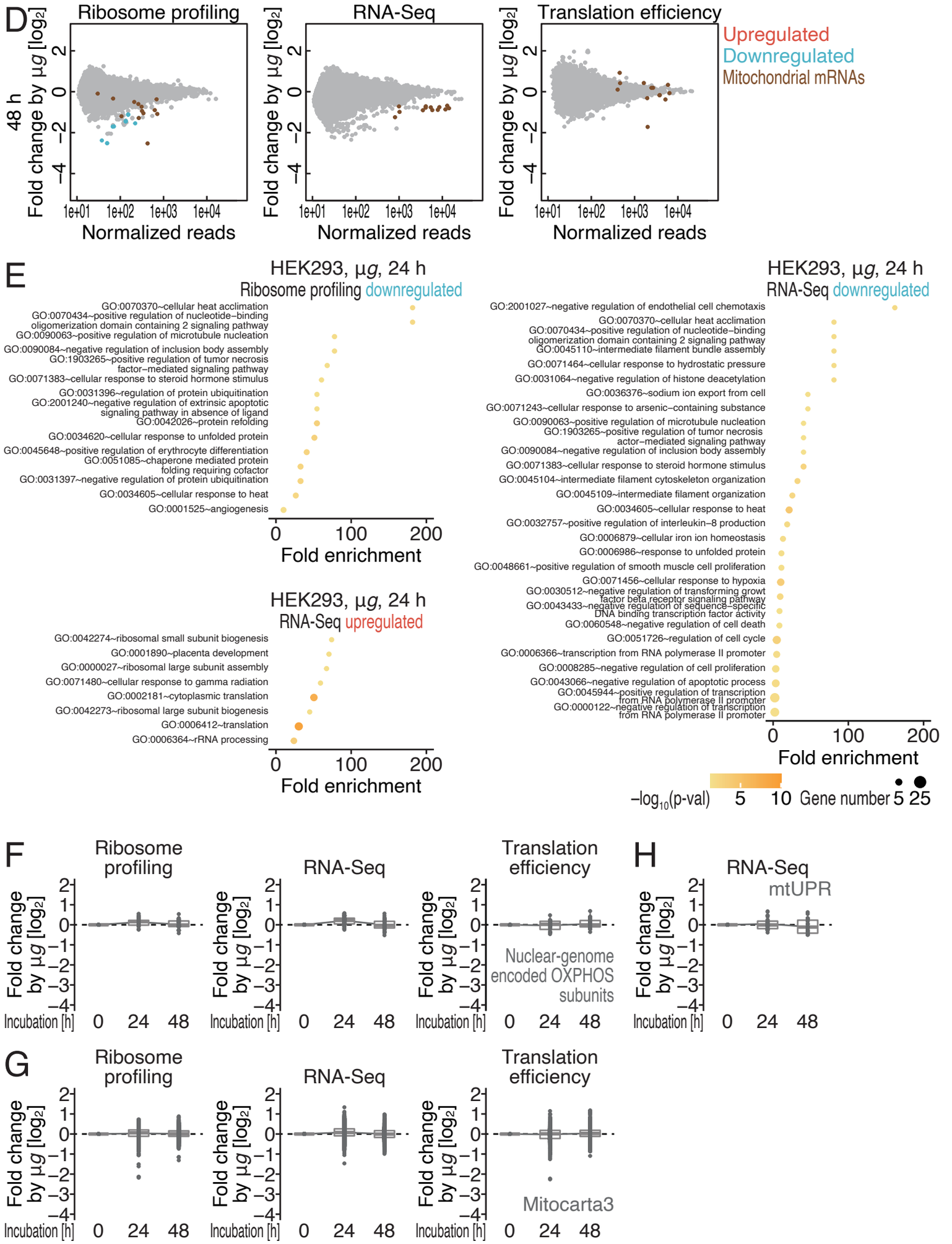

Figure S1 Wakigawa, Kimura *et al.* (2023)

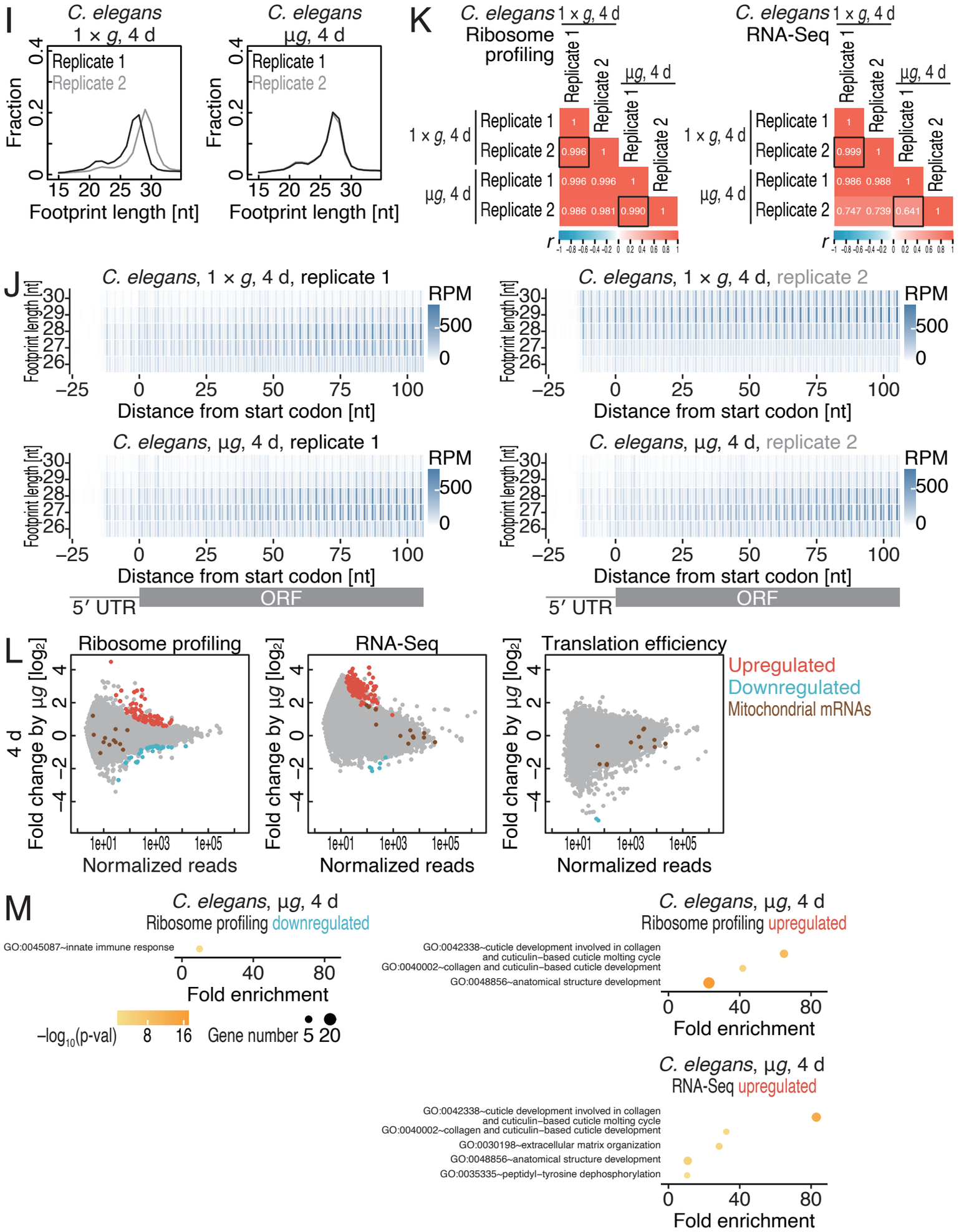

Figure S1 Wakigawa, Kimura *et al.* (2023)

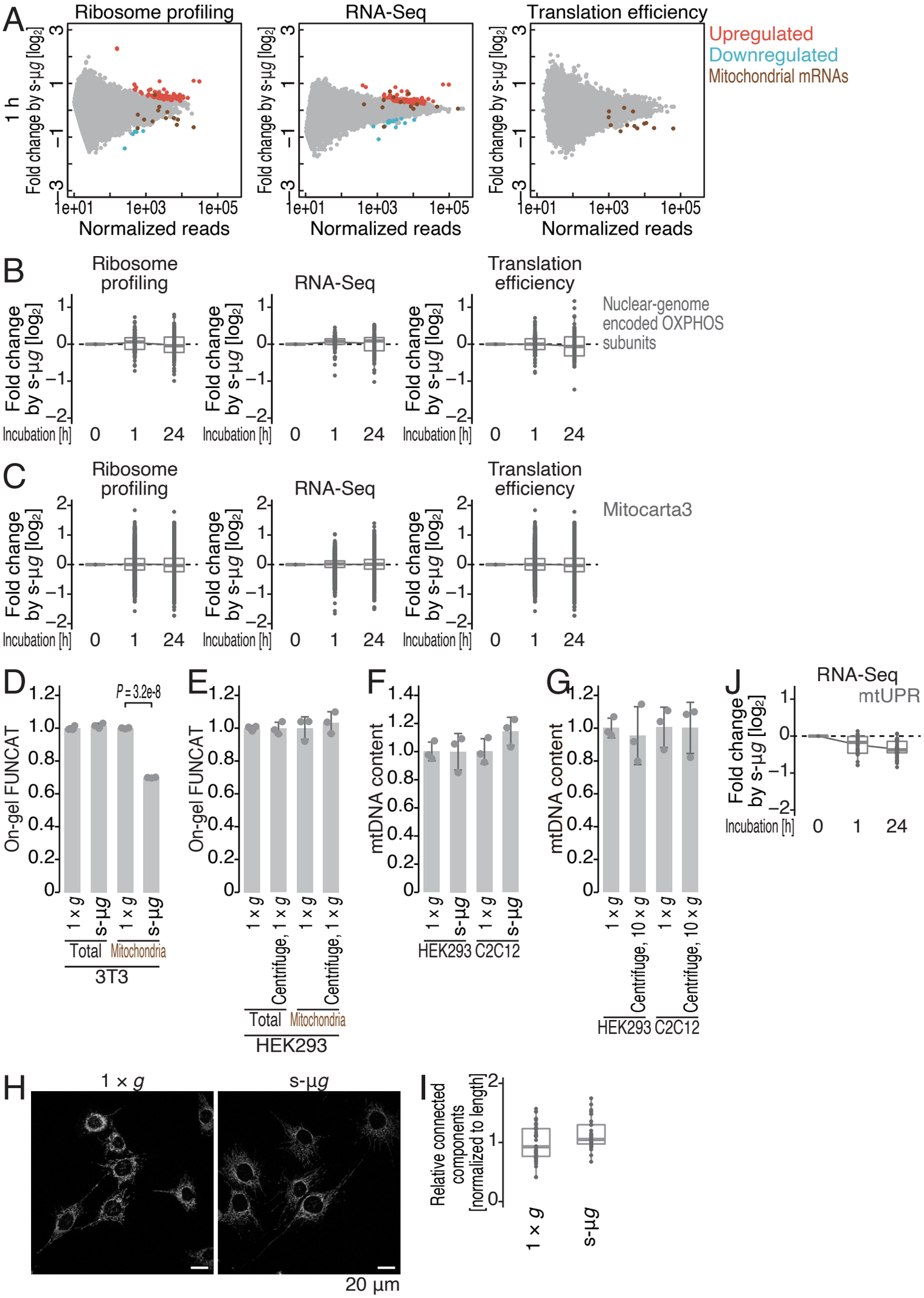

Figure S2 Wakigawa, Kimura *et al.* (2023)

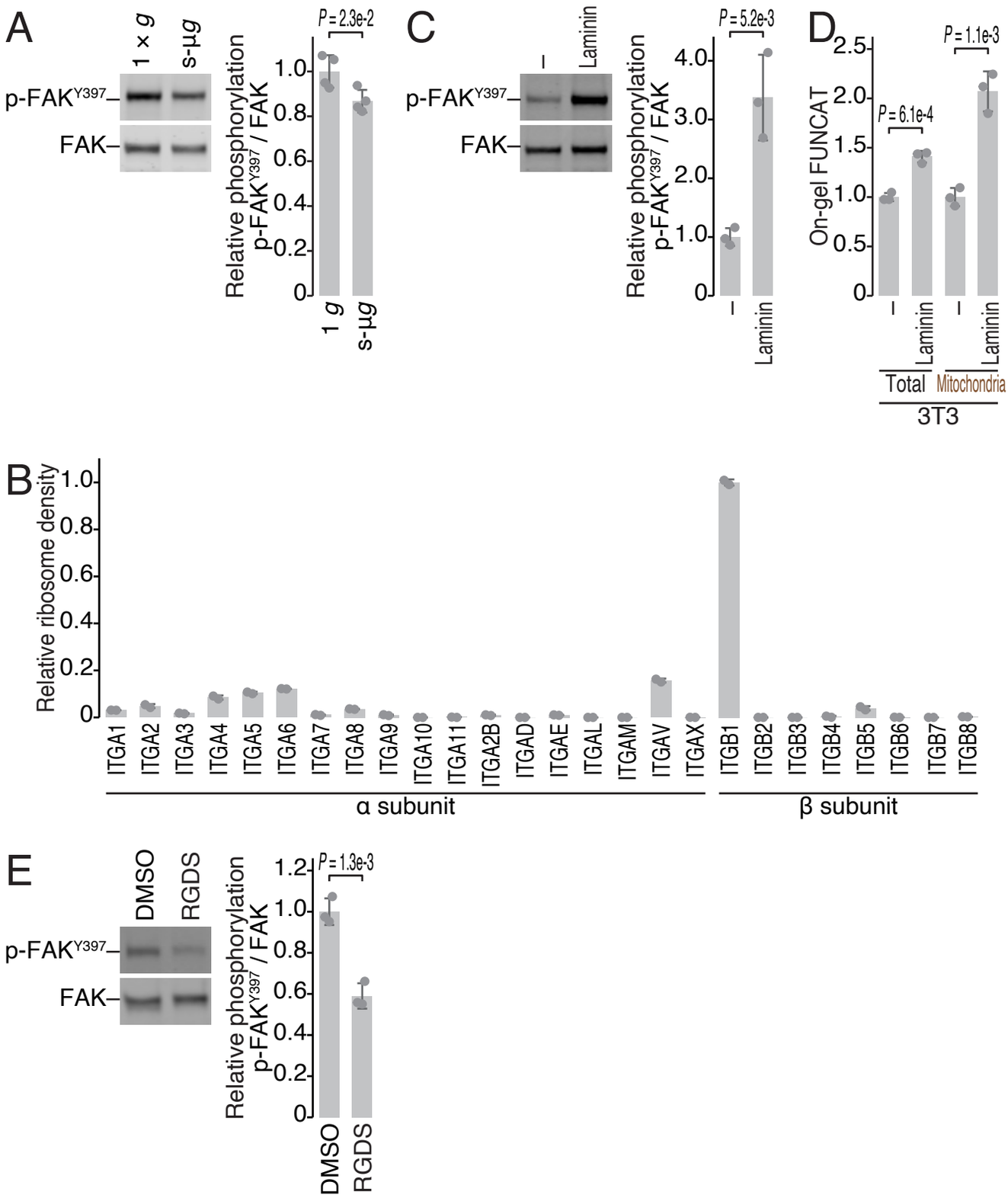

Figure S3 Wakigawa, Kimura *et al.* (2023)

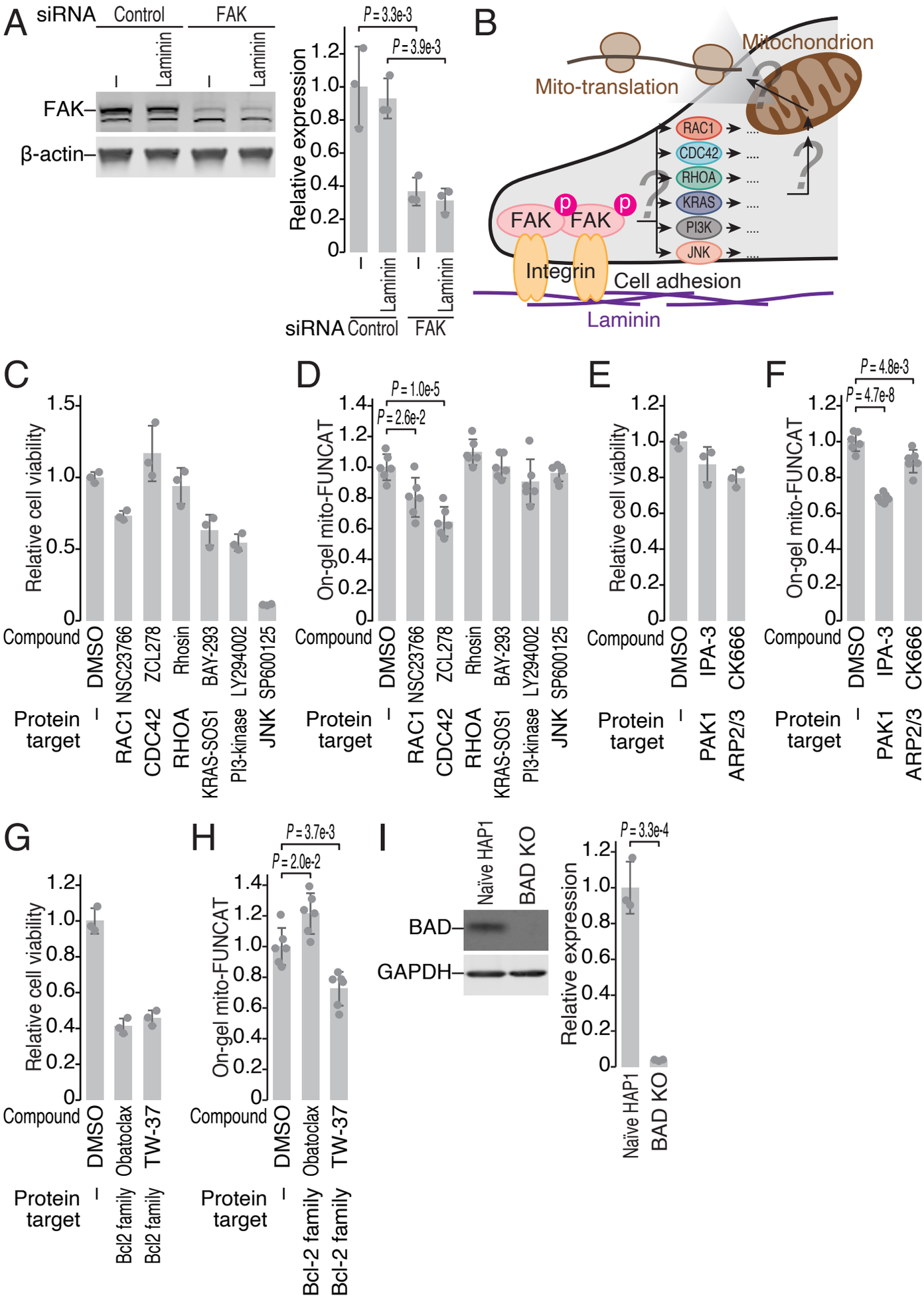

Figure S4 Wakigawa, Kimura *et al.* (2023)

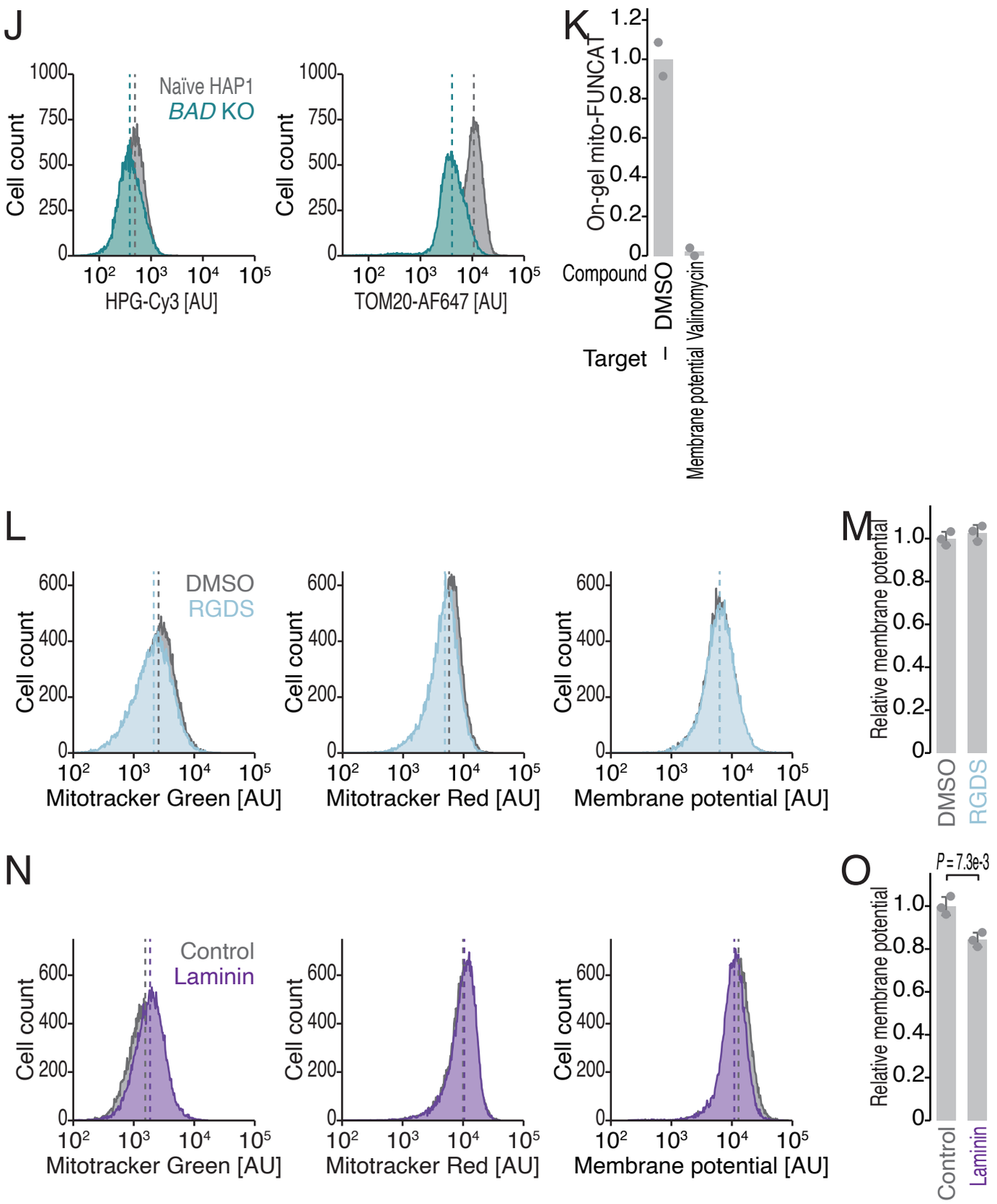

Figure S4 Wakigawa, Kimura *et al.* (2023)

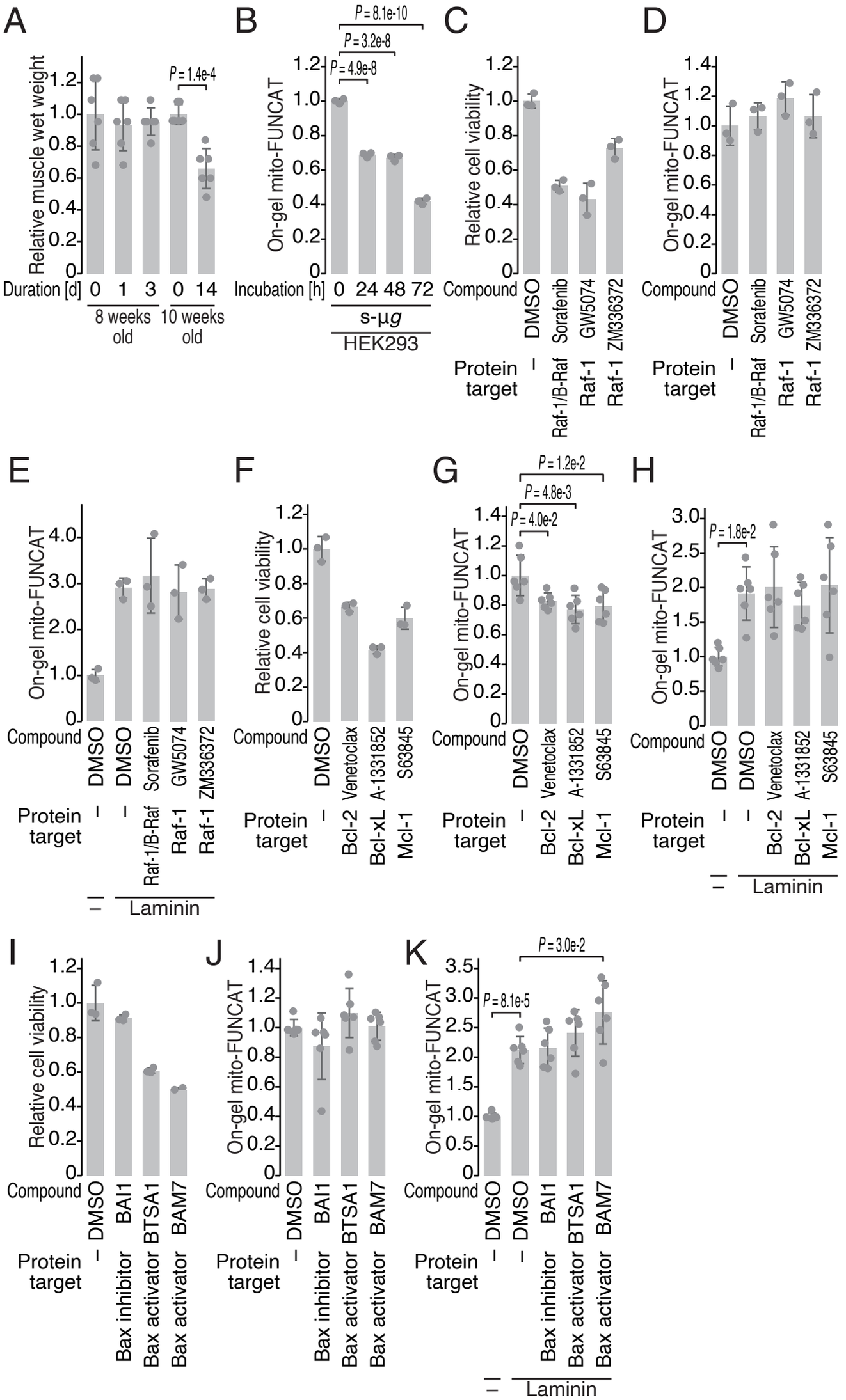

Figure S5 Wakigawa, Kimura *et al.* (2023)

Library	Samples	Condition	Replicate	Cytoribosome footprint length	A-site position offsets for cytoribome footprrints	Mitoribosome footprint length	A-site position offsets for mitoribosome footprints
L1	HEK293	1 *g* for 24 h in the ISS	Replicate1	20, 21, 22, 23, 24, 25, 26, 27, 28, 29, 30, 31	15, 15, 15, 15, 11, 12, 13, 14, 15, 15, 15, 15	15, 16, 17, 18, 19, 20	15, 15, 15, 15, 15, 15
L2	HEK293	1 *g* for 24 h in the ISS	Replicate2	20, 21, 22, 23, 24, 25, 26, 27, 28, 29, 30, 31	15, 15, 15, 15, 11, 12, 13, 14, 15, 15, 15, 15	15, 16, 17, 18, 19, 20	15, 15, 15, 15, 15, 15
L3	HEK293	1 *g* for 48 h in the ISS	Replicate1	20, 21, 22, 23, 24, 25, 26, 27, 28, 29, 30, 31	15, 15, 15, 15, 11, 12, 13, 14, 15, 15, 15, 15	15, 16, 17, 18, 19, 20	15, 15, 15, 15, 15, 15
L4	HEK293	1 *g* for 48 h in the ISS	Replicate2	20, 21, 22, 23, 24, 25, 26, 27, 28, 29, 30, 31	15, 15, 15, 15, 11, 12, 13, 14, 15, 15, 15, 15	15, 16, 17, 18, 19, 20	15, 15, 15, 15, 15, 15
L5	HEK293	µ*g* for 24 h in the ISS	Replicate1	20, 21, 22, 23, 24, 25, 26, 27, 28, 29, 30, 31	15, 15, 15, 15, 11, 12, 13, 14, 15, 15, 15, 15	15, 16, 17, 18, 19, 20	15, 15, 15, 15, 15, 15
L6	HEK293	µ*g* for 24 h in the ISS	Replicate2	20, 21, 22, 23, 24, 25, 26, 27, 28, 29, 30, 31	15, 15, 15, 15, 11, 12, 13, 14, 15, 15, 15, 15	15, 16, 17, 18, 19, 20	15, 15, 15, 15, 15, 15
L7	HEK293	µ*g* for 48 h in the ISS	Replicate1	20, 21, 22, 23, 24, 25, 26, 27, 28, 29, 30, 31	15, 15, 15, 15, 11, 12, 13, 14, 15, 15, 15, 15	15, 16, 17, 18, 19, 20	15, 15, 15, 15, 15, 15
L8	HEK293	µ*g* for 48 h in the ISS	Replicate2	20, 21, 22, 23, 24, 25, 26, 27, 28, 29, 30, 31	15, 15, 15, 15, 11, 12, 13, 14, 15, 15, 15, 15	15, 16, 17, 18, 19, 20	15, 15, 15, 15, 15, 15
L9	*C. elegans*	1 *g* for 4 d in the ISS	Replicate1	20, 21, 22, 23, 24, 25, 26, 27, 28, 29, 30	14, 15, 15, 15, 13, 13, 14, 15, 15, 15, 15	25, 26, 27, 28, 29, 30, 31, 32, 33, 34, 35, 36, 37, 38, 39, 40	15, 15, 15, 15, 15, 15, 15, 15, 15, 15, 15, 15, 15, 15, 15, 15
L10	*C. elegans*	1 *g* for 4 d in the ISS	Replicate2	20, 21, 22, 23, 24, 25, 26, 27, 28, 29, 30	14, 15, 15, 15, 13, 13, 14, 15, 15, 15, 15	25, 26, 27, 28, 29, 30, 31, 32, 33, 34, 35, 36, 37, 38, 39, 40	15, 15, 15, 15, 15, 15, 15, 15, 15, 15, 15, 15, 15, 15, 15, 15
L11	*C. elegans*	µ*g* for 4 d in the ISS	Replicate1	20, 21, 22, 23, 24, 25, 26, 27, 28, 29, 30	14, 15, 15, 15, 13, 13, 14, 15, 15, 15, 15	25, 26, 27, 28, 29, 30, 31, 32, 33, 34, 35, 36, 37, 38, 39, 40	15, 15, 15, 15, 15, 15, 15, 15, 15, 15, 15, 15, 15, 15, 15, 15
L12	*C. elegans*	µ*g* for 4 d in the ISS	Replicate2	20, 21, 22, 23, 24, 25, 26, 27, 28, 29, 30	14, 15, 15, 15, 13, 13, 14, 15, 15, 15, 15	25, 26, 27, 28, 29, 30, 31, 32, 33, 34, 35, 36, 37, 38, 39, 40	15, 15, 15, 15, 15, 15, 15, 15, 15, 15, 15, 15, 15, 15, 15, 15
L13	HEK293	1 *g* on the ground	Replicate1	27, 28, 29, 30, 31, 32	15, 15, 15, 15, 15, 15	27, 28, 29, 30, 31, 32	15, 15, 15, 15, 15, 15
L14	HEK293	1 *g* on the ground	Replicate2	27, 28, 29, 30, 31, 32	15, 15, 15, 15, 15, 15	27, 28, 29, 30, 31, 32	15, 15, 15, 15, 15, 15
L15	HEK293	s-µ*g* for 1 h on the ground	Replicate1	27, 28, 29, 30, 31, 32	15, 15, 15, 15, 15, 15	27, 28, 29, 30, 31, 32	15, 15, 15, 15, 15, 15
L16	HEK293	s-µ*g* for 24 h on the ground	Replicate1	27, 28, 29, 30, 31, 32	15, 15, 15, 15, 15, 15	27, 28, 29, 30, 31, 32	15, 15, 15, 15, 15, 15
L17	HEK293	1 *g* with laminin-coating on the ground	Replicate1	20, 21, 22, 23, 24, 25, 26, 27, 28, 29, 30, 31	15, 15, 15, 15, 15, 15, 15, 15, 15, 15, 15, 15	18, 19, 20, 21, 22, 23, 24, 25, 26, 27, 28, 29, 30, 31, 32, 33, 34, 35	14, 14, 14, 15, 15, 13, 13, 13, 13, 14, 14, 15, 15, 15, 15, 15, 16, 16
L18	HEK293	1 *g* with laminin-coating on the ground	Replicate2	20, 21, 22, 23, 24, 25, 26, 27, 28, 29, 30, 31	15, 15, 15, 15, 15, 15, 15, 15, 15, 15, 15, 15	18, 19, 20, 21, 22, 23, 24, 25, 26, 27, 28, 29, 30, 31, 32, 33, 34, 35	14, 14, 14, 15, 15, 13, 13, 13, 13, 14, 14, 15, 15, 15, 15, 15, 16, 16
L19	HEK293	*s*-µ*g* with laminin-coating for 1 h on the ground	Replicate1	20, 21, 22, 23, 24, 25, 26, 27, 28, 29, 30, 31	15, 15, 15, 15, 15, 15, 15, 15, 15, 15, 15, 15	18, 19, 20, 21, 22, 23, 24, 25, 26, 27, 28, 29, 30, 31, 32, 33, 34, 35	14, 14, 14, 15, 15, 13, 13, 13, 13, 14, 14, 15, 15, 15, 15, 15, 16, 16
L20	HEK293	*s*-µ*g* with laminin-coating for 24 h on the ground	Replicate1	20, 21, 22, 23, 24, 25, 26, 27, 28, 29, 30, 31	15, 15, 15, 15, 15, 15, 15, 15, 15, 15, 15, 15	17, 18, 19, 20, 21, 22, 24, 25, 26, 27, 28, 29, 30, 31, 32, 33, 34, 35	14, 14, 14, 14, 15, 15, 13, 13, 13, 14, 14, 15, 15, 15, 15, 15, 16, 16
L21	Mouse soleus	Control 8 weeks old	Replicate1	20, 21, 22, 23, 24, 25, 26, 27, 28, 29, 30, 31, 32	15, 15, 15, 15, 12, 13, 13, 14, 15, 15, 15, 15	28, 29, 30, 31, 32, 33, 34, 35, 36	17, 17, 18, 18, 18, 18, 18, 18, 18
L22	Mouse soleus	Control 8 weeks old	Replicate2	20, 21, 22, 23, 24, 25, 26, 27, 28, 29, 30, 31, 32	15, 15, 15, 15, 12, 13, 13, 14, 15, 15, 15, 15	28, 29, 30, 31, 32, 33, 34, 35, 36	17, 17, 18, 18, 18, 18, 18, 18, 18
L23	Mouse soleus	Control 8 weeks old	Replicate3	20, 21, 22, 23, 24, 25, 26, 27, 28, 29, 30, 31, 32	15, 15, 15, 15, 12, 13, 13, 14, 15, 15, 15, 15	28, 29, 30, 31, 32, 33, 34, 35, 36	17, 17, 18, 18, 18, 18, 18, 18, 18
L24	Mouse soleus	MMS for 1 d	Replicate1	20, 21, 22, 23, 24, 25, 26, 27, 28, 29, 30, 31, 32	15, 15, 15, 15, 12, 13, 13, 14, 15, 15, 15, 15	28, 29, 30, 31, 32, 33, 34, 35, 36	17, 17, 18, 18, 18, 18, 18, 18, 18
L25	Mouse soleus	MMS for 1 d	Replicate2	20, 21, 22, 23, 24, 25, 26, 27, 28, 29, 30, 31, 32	15, 15, 15, 15, 12, 13, 13, 14, 15, 15, 15, 15	28, 29, 30, 31, 32, 33, 34, 35, 36	17, 17, 18, 18, 18, 18, 18, 18, 18
L26	Mouse soleus	MMS for 1 d	Replicate3	20, 21, 22, 23, 24, 25, 26, 27, 28, 29, 30, 31, 32	15, 15, 15, 15, 12, 13, 13, 14, 15, 15, 15, 15	28, 29, 30, 31, 32, 33, 34, 35, 36	17, 17, 18, 18, 18, 18, 18, 18, 18
L27	Mouse soleus	MMS for 3 d	Replicate1	20, 21, 22, 23, 24, 25, 26, 27, 28, 29, 30, 31, 32	15, 15, 15, 15, 12, 13, 13, 14, 15, 15, 15, 15	28, 29, 30, 31, 32, 33, 34, 35, 36	17, 17, 18, 18, 18, 18, 18, 18, 18
L28	Mouse soleus	MMS for 3 d	Replicate2	20, 21, 22, 23, 24, 25, 26, 27, 28, 29, 30, 31, 32	15, 15, 15, 15, 12, 13, 13, 14, 15, 15, 15, 15	28, 29, 30, 31, 32, 33, 34, 35, 36	17, 17, 18, 18, 18, 18, 18, 18, 18
L29	Mouse soleus	MMS for 3 d	Replicate3	20, 21, 22, 23, 24, 25, 26, 27, 28, 29, 30, 31, 32	15, 15, 15, 15, 12, 13, 13, 14, 15, 15, 15, 15	28, 29, 30, 31, 32, 33, 34, 35, 36	17, 17, 18, 18, 18, 18, 18, 18, 18
L30	Mouse soleus	Control 10 weeks old	Replicate1	20, 21, 22, 23, 24, 25, 26, 27, 28, 29, 30, 31, 32	15, 15, 15, 15, 12, 13, 13, 14, 15, 15, 15, 15	28, 29, 30, 31, 32, 33, 34, 35, 36	17, 17, 18, 18, 18, 18, 18, 18, 18
L31	Mouse soleus	Control 10 weeks old	Replicate2	20, 21, 22, 23, 24, 25, 26, 27, 28, 29, 30, 31, 32	15, 15, 15, 15, 12, 13, 13, 14, 15, 15, 15, 15	28, 29, 30, 31, 32, 33, 34, 35, 36	17, 17, 18, 18, 18, 18, 18, 18, 18
L32	Mouse soleus	MMS for 14 d	Replicate1	20, 21, 22, 23, 24, 25, 26, 27, 28, 29, 30, 31, 32	15, 15, 15, 15, 12, 13, 13, 14, 15, 15, 15, 15	28, 29, 30, 31, 32, 33, 34, 35, 36	17, 17, 18, 18, 18, 18, 18, 18, 18
L33	Mouse soleus	MMS for 14 d	Replicate2	20, 21, 22, 23, 24, 25, 26, 27, 28, 29, 30, 31, 32	15, 15, 15, 15, 12, 13, 13, 14, 15, 15, 15, 15	28, 29, 30, 31, 32, 33, 34, 35, 36	17, 17, 18, 18, 18, 18, 18, 18, 18